



Mapping and quantifying *Sargassum* distribution and coverage in the Central West Atlantic using MODIS observations

Mengqiu Wang, Chuanmin Hu *

College of Marine Science, University of South Florida, 140 Seventh Avenue South, St. Petersburg, FL 33701, USA



ARTICLE INFO

Article history:

Received 18 January 2016

Received in revised form 17 April 2016

Accepted 27 April 2016

Available online 25 June 2016

Keywords:

Sargassum

Remote sensing

MODIS

FAI

AFAI

Cloud

Cloud shadow

Feature extraction

Surface fitting

ABSTRACT

Sargassum washing ashore on the beaches of the Caribbean Islands since 2011 has caused problems for the local environments, tourism, and economies. Although preliminary results of *Sargassum* distributions in the nearby oceans have been obtained using measurements from the Medium Resolution Imaging Spectrometer (MERIS), MERIS stopped functioning in 2012, and detecting and quantifying *Sargassum* distributions still face technical challenges due to ambiguous pixels from clouds, cloud shadows, cloud adjacency effect, and large-scale image gradient. In this paper, a novel approach is developed to detect *Sargassum* presence and to quantify *Sargassum* coverage using the Moderate Resolution Imaging Spectroradiometer (MODIS) alternative floating algae index (AFAI), which examines the red-edge reflectance of floating vegetation. This approach includes three basic steps: 1) classification of *Sargassum*-containing pixels through correction of large-scale gradient, masking clouds and cloud shadows, and removal of ambiguous pixels; 2) linear unmixing of *Sargassum*-containing pixels; and, 3) statistics of *Sargassum* area coverage in pre-defined grids at monthly, seasonal, and annual intervals. In the absence of direct field measurements to validate the results, limited observations from the Hyperspectral Imager for the Coastal Ocean (HICO) measurements and numerous local reports support the conclusion that the elevated AFAI signals are due to the presence of *Sargassum* instead of other floating materials, and various sensitivity analyses are used to quantify the uncertainties in the derived *Sargassum* area coverage. The approach was applied to MODIS observations between 2000 and 2015 over the Central West Atlantic (CWA) region (0–22°N, 63–38°W) to derive the spatial and temporal distribution patterns as well as the total area coverage of *Sargassum*. Results indicate that the first widespread *Sargassum* distribution event occurred in 2011, consistent with previous MERIS findings. Since 2011, only 2013 showed a minimal *Sargassum* coverage similar to the period of 2000 to 2010; all other years showed significantly more coverage. More alarmingly, the summer months of 2015 showed mean coverage of >2000 km², or about 4 times of the summer 2011 coverage and 20 times of the summer 2000 to 2010 coverage. Analysis of several environmental variables provided some hints on the reasons causing the inter-annual changes after 2010, yet further multi-disciplinary research (including in situ measurements) is required to understand such changes and long-term trends in *Sargassum* coverage.

© 2016 Elsevier Inc. All rights reserved.

1. Introduction

Since 2011, massive beaching events of the pelagic *Sargassum* macroalgae have occurred frequently on the Lesser Antilles Islands in the southern Caribbean (Fig. 1), significantly impacting local environments, tourism, fisheries, and economies (<http://mission-blue.org/2014/10/sargassum-inundates-the-beaches-of-the-caribbean/>; Gower, Young, & King, 2013; Maurer, De Neef, & Stapleton, 2015). Concurrent beaching events in western Africa and northern Brazil have also been reported (Oyesiku & Egungyomi, 2015; Széchy, Guedes, Baeta-Neves, & Oliveira, 2012). While pelagic *Sargassum* serves as an important habitat and refuge for many marine organisms in the open-ocean environment (Council, 2002; Rooker, Turner, & Holt, 2006; Witherington, Hirama, &

Hardy, 2012), excessive beaching poses significant environmental and profound economic problems. For example, over \$2.91 million have been spent annually on the cleanup of *Sargassum* from Texas beaches (Webster & Linton, 2013). Despite the enormous efforts of local management in response to these beaching events, our knowledge about these blooms is limited. For example: Where do *Sargassum* blooms initiate? How much *Sargassum* is present in the oceans? What causes these blooms and their inter-annual changes? How do these blooms impact the ocean's biogeochemistry and ecology? Indeed, to date, the only published remote sensing works used Medium Resolution Imaging Spectrometer (MERIS) observations to document the *Sargassum* distributions and abundance in the Intra-Americas Sea and the central Atlantic between 2002 and 2011 (Gower & King, 2011; Gower et al., 2013). However, as MERIS stopped functioning in early 2012, there is virtually no information on the *Sargassum* distribution or abundance in the Caribbean, the greater Intra-Americas Sea, or nearby oceans after 2011

* Corresponding author.

E-mail address: huc@usf.edu (C. Hu).

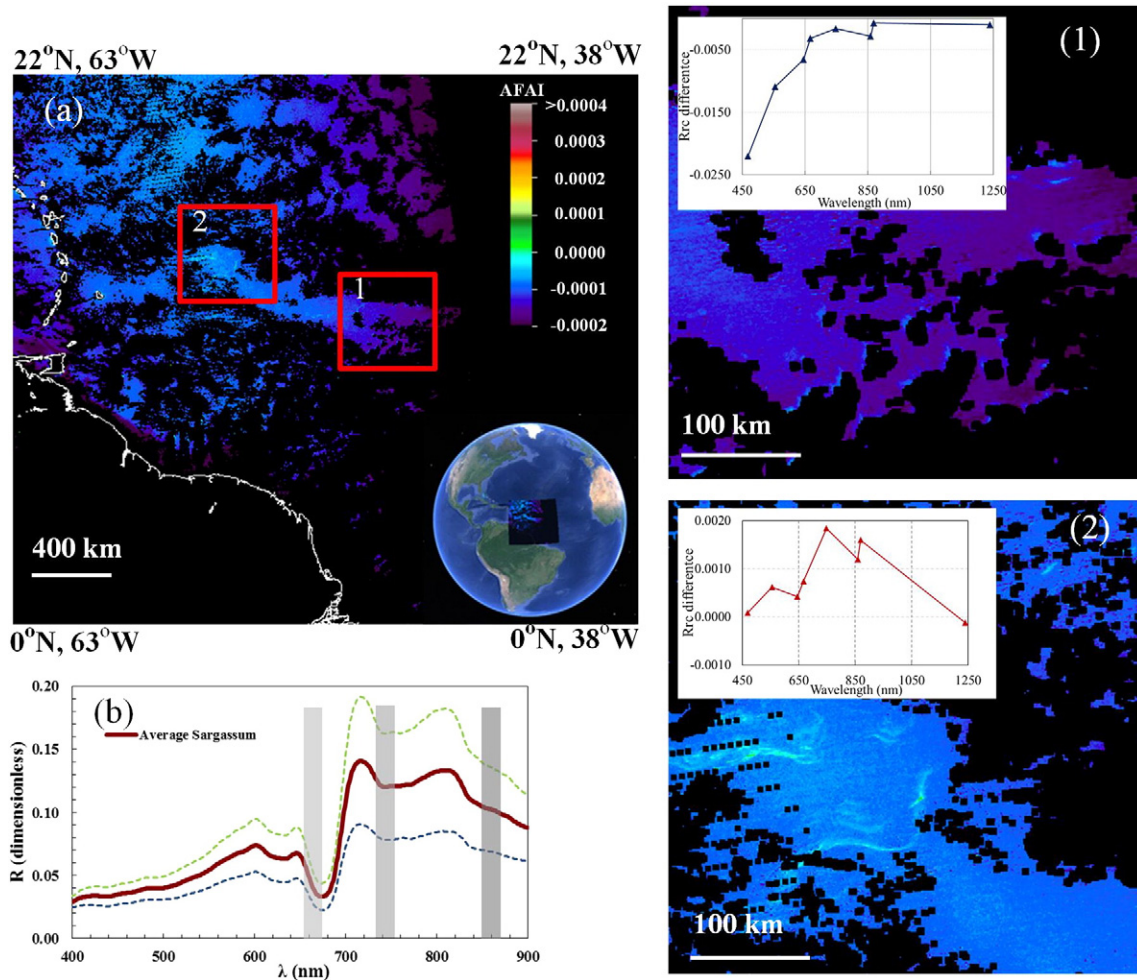


Fig. 1. MODIS/Aqua AFAI image (a) on 1 January 2015 (17:05 GMT) over the CWA showing surface slicks (box 2) with enhanced near infrared (NIR) reflectance. Black color indicates land or clouds or sunglint, representing no valid observation. The blue-colored features near the cloud edge (box 1), although easily identified as non-Sargassum through visual inspection, make accurate quantification of Sargassum coverage very difficult with automatic methods because they can be falsely treated as Sargassum-containing pixels. Red crosses mark the location of the cloud shadow and Sargassum pixels whose R_{rc} difference spectra (compared to the nearby water pixels) are shown in box 1 and box 2, respectively. The surface reflectance spectra (R , dimensionless) of Sargassum mats measured in the Gulf of Mexico and off Bermuda using a hand-held spectrometer are shown in (b). The thick solid line represents the mean of >50 measurements while the dashed lines indicate 2 times of standard deviation. Also overlaid are the three MODIS bands centered at 667, 748, and 869 nm, which are used to calculate AFAI.

because of the loss of MERIS. Furthermore, the methods used in the MERIS-based study to detect and quantify Sargassum require refinements (see Section 2). Because these questions remain unanswered, the effort to broaden and continue further research, through the refinement of MERIS-based observations, and while exploring the possibility of using other satellite instruments, becomes crucial.

In 2009, Hu (2009) developed a floating algae index (FAI) using data collected by the Moderate Resolution Imaging Spectroradiometer (MODIS) to detect and trace the *Ulva prolifera* macroalgae blooms in the Yellow Sea near Qingdao, China (He, Liu, Yu, Li, & Hu, 2011; Hu et al., 2010a). Because FAI was designed using the vegetation red-edge reflectance in the near infrared, it can be used to detect any floating vegetation including Sargassum (Hu, Feng, Hardy, & Hochberg, 2015). In 2010, in order to help monitor potential Sargassum beaching events on the Lesser Antilles Islands in the southern Caribbean, FAI was implemented to generate MODIS FAI imagery covering the Central West Atlantic (CWA) region ($0\text{--}22^{\circ}\text{N}$, $63\text{--}38^{\circ}\text{W}$) in near real-time through a Virtual Antenna System (VAS) (Hu, Barnes, Murch, & Carlson, 2014). The system has been running operationally with daily updates in near real-time (within 4–6 h of the satellite overpass). However, because there is no effective cloud-masking method for FAI, clouds are not masked in the imagery. Although Sargassum slicks can be visually differentiated from clouds in FAI imagery with a trained eye, it is difficult for visual interpretation by average users, as both Sargassum slicks and

clouds show high FAI values. To overcome this difficulty, an alternative FAI (AFAI) was developed (where clouds can be masked through band combinations), and data was produced over the whole MODIS time series (see below). Fig. 1 shows an example of the AFAI imagery generated and distributed in near real-time.

AFAI imagery allows for simple interpretation by a layperson to identify surface slicks of floating vegetation. When combined with surface current velocity estimates from the Hycom hydrodynamics model (all available through a simple click on a customized web portal <http://optics.marine.usf.edu/projects/SaWS.html> with full Google-Earth compatibility), the AFAI imagery has provided timely information on the location of large Sargassum slicks as well as their movement speed and direction to many local groups and individuals (Hu et al., 2014). However, several difficulties emerged when attempting to derive long-term statistics of Sargassum distribution and abundance using near real-time imagery: 1) frequent cloud cover made the valid data rather scarce (note the location of this region's proximity to the Inter Tropical Convergence Zone (ITCZ)) (Wylie, Jackson, Menzel, & Bates, 2005); 2) although it is relatively straightforward to identify Sargassum slicks through visual inspection, because false positive detection often results from cloud shadow contamination it is difficult to automate such a detection; 3) the large-scale AFAI gradient across the image scene makes it difficult to apply threshold-based segmentation; and, 4) each identified Sargassum-containing pixel may contain varying

proportions of *Sargassum*, leading to biased statistics if each *Sargassum*-containing pixel is treated equally.

Hence, given the challenges in quantitative assessment of *Sargassum* distributions, area coverage, long-term trends, and the pressing need of such knowledge in order to understand the potential causes of the trend and to help make management decisions, the objectives of this study, based on the existing MODIS AFAI imagery, are to:

- 1) develop a practical and objective method to quantify *Sargassum* distribution and area coverage in the Central West Atlantic using MODIS observations; and,
- 2) establish a long-term (2000–2015) time series of *Sargassum* distribution patterns and area coverage in the study region to quantify the long-term trend.

As this is primarily a methodology development paper, rather than following a traditional structure, the paper is organized in a way to first provide some background on *Sargassum* detection, then detail all steps in the method, and finally present a time series of *Sargassum* distributions. While the focus of this study is on the development of methodology and establishment of long-term time series, a preliminary analysis of several environmental variables is also undertaken in an attempt to understand these long-term patterns.

2. Sargassum remote sensing: What is available and what is not?

Gower, Hu, Borstad, and King (2006) first demonstrated that pelagic *Sargassum* (*Sargassum natans* and *Sargassum fluitans*) can be detected from satellite imagery based on elevated NIR reflectance (the red-edge effect, i.e., enhanced reflectance between 700 and 730 nm). This detection principle was applied to MERIS Maximum Chlorophyll Index (MCI (Gower, King, Borstad, & Brown, 2005)) (Gower et al., 2006), and later to MODIS FAI (Hu, 2009). Based on the MERIS MCI products, Gower and King (2011) first generated *Sargassum* distribution maps for the Gulf of Mexico (GOM) and Sargasso Sea between 2002 and 2008. They were later improved by extending coverage to include the central Atlantic with data up to 2011 in an attempt to explain the potential source of the 2011 *Sargassum* bloom in the Caribbean (Gower et al., 2013). When generating the monthly *Sargassum* distribution maps, for each of the pre-defined 5-km grids within the area of interest, the maximum MCI was used to represent that grid. Then, the maximum MCI value during the entire month was used to represent the monthly MCI value for that grid. Monthly maps derived in this manner potentially contain three error sources: 1) MCI was obtained from top-of-atmosphere (TOA) radiance, instead of atmospherically corrected reflectance, leading to uncertainties in deriving a universal threshold for *Sargassum* detection; 2) errors in TOA radiance-based cloud-masking; and 3) the use of maximum MCI instead of mean MCI within the 5-km grid during a month may overestimate *Sargassum* abundance.

Hu (2009) showed that MODIS FAI can also be used to detect macroalgae blooms. MODIS FAI and AFAI were implemented to detect and trace *Sargassum* blooms in near real-time over the CWA in 2010 (Hu et al., 2014) but has since been back processed to 2000 to include all MODIS data for the region. Compared to MERIS MCI, MODIS AFAI provides a comparable and potentially better alternative because MODIS is onboard both Aqua and Terra satellites (afternoon and morning passes, respectively) and each MODIS swath (2330 km) is approximately twice that of a MERIS swath (1150 km). Although the near real-time MODIS AFAI imagery has provided valuable information on the *Sargassum* location and movement, its interpretation was primarily based on visual inspection. Due to technical difficulties such as discriminating ambiguous pixels from clouds, cloud shadows, cloud adjacency effects, and removing large-scale image gradients, there has not been any automatic detection, delineation, or use of MODIS AFAI to generate long-term statistics.

To date, most macroalgae delineation methods (through the use of MCI, FAI, Normalized Difference Vegetation Index (NDVI), or other

similar data products) are threshold-based segmentation methods that all suffer from cross-scene large-scale image gradient. Several attempts have been made to use a global-scope threshold for image segmentation in recent studies. In 2009, Shi and Wang (2009) developed a floating macroalgae delineation method producing Normalized Difference Algae Index (NDAI) products which are similar to NDVI products, but a Rayleigh correction is applied to TOA reflectance to remove the molecular scattering effects before NDAI is calculated. The image is first classified into “algae” and “non-algae” classes using the median value of the NDAI scene, then the ocean background pixel value is determined from the mean value of the “non-algae” pixels in a 10 × 10 pixel window centered on the given “algae” pixel (Shi & Wang, 2009). The potential problems in this method are: 1) that the mean value may be affected by the high signal values of the algae pixels; 2) the 10 × 10 pixel window could be largely or even completely contaminated by algae pixels; and, 3) that the scene-wide NDAI median value may not be able to provide a good classification of the algae pixels (Garcia, Fearns, Keesing, & Liu, 2013). The main idea is to obtain the background ocean signal through image processing so that local macroalgae signals can be scaled against the cross-image gradient. To overcome these issues, a ‘difference image’ was proposed by Keesing, Liu, Fearns, and Garcia in 2011 and is computed by subtracting a background ocean image from the original image. Called the Scaled Algae Index (SAI) method, Keesing, Liu, Fearns, and Garcia (2011) proposed it to quantify *U. prolifera* macroalgae blooms in the Yellow Sea from MODIS NDVI images. The method used a 25 × 25 pixel median filter to determine the background water signal and applied a local threshold segmentation, based on the statistical distribution in the 25 × 25 pixel window, centered on the pixel of interest. The method was further modified in Garcia et al. (2013) to select the optimal window size and segmentation threshold. Due to variability of the feature distribution in the median filter window, the window size and the threshold often need to be tuned by a human expert to achieve satisfactory performance. In short, although visual detection is straightforward through one of the indexes, automatic detection and quantification of macroalgae blooms are still problematic when long-term time series data are desired. Another difficulty is that these indexes only detect the red-edge reflectance and thus not able to spectrally differentiate *Sargassum* from other floating materials (Dierssen, Chlus, & Russell, 2015; Hu et al., 2015). While the latter requires hyperspectral data that are mostly unavailable from current satellites, the former is addressed using the approach developed in this study.

3. Data sources and processing methods

Although the near real-time monitoring of *Sargassum* slicks started in 2010 (Hu et al., 2014), the development of a complete time series MODIS data set, covering the CWA between April 2000 and October 2015, required downloading all relevant data from the U.S. National Aeronautics and Space Administration (NASA) Goddard Space Flight Center (<http://oceancolor.gsfc.nasa.gov>) which were subsequently processed using the software package SeaDAS (version 7.0.2) to generate Rayleigh-corrected reflectance (Rrc) data for each spectral band (Hu, 2009). Both MODIS/Terra (MODIST) and MODIS/Aqua (MODISA) data were downloaded and processed. The Rrc data were then used to calculate FAI for each pixel (Hu, 2009):

$$\begin{aligned} \text{FAI} &= R_{\text{rc,NIR}} - R'_{\text{rc,NIR}} \\ R'_{\text{rc,NIR}} &= R_{\text{rc,RED}} + (R_{\text{rc,SWIR}} - R_{\text{rc,RED}}) \times (\lambda_{\text{NIR}} - \lambda_{\text{RED}}) / (\lambda_{\text{SWIR}} - \lambda_{\text{RED}}), \end{aligned} \quad (1)$$

where the subscripts RED, NIR and short-wave infrared (SWIR) represent the spectral bands. FAI is the difference between $R_{\text{rc,NIR}}$ and the baseline reflectance $R'_{\text{rc,NIR}}$ derived from the linear interpolation between the red and SWIR bands. For MODIS FAI calculations, $\lambda_{\text{RED}} = 645 \text{ nm}$, $\lambda_{\text{NIR}} = 859 \text{ nm}$, and $\lambda_{\text{SWIR}} = 1240 \text{ nm}$. The FAI product provides a quick and easy way to visualize surface floating algae. However, due to lack of an effective cloud-masking algorithm, only people with

training can differentiate floating algae slicks from cloud patches and other artifacts. This represents a major hurdle for an average person to interpret the images. To overcome this difficulty, the AFAI product was generated using the same FAI design but using different spectral bands ($\lambda_{\text{RED}} = 667 \text{ nm}$, $\lambda_{\text{NIR}} = 748 \text{ nm}$, $\lambda_{\text{SWIR}} = 869 \text{ nm}$). Note that although 869 nm is in the NIR spectral range, for simplicity and consistency it is still termed as "SWIR".

Although AFAI has a lower spatial resolution (1-km) compared to FAI (250-m), the 1-km bands used in calculating AFAI have much higher signal-to-noise ratios (SNRs) than the 250-m bands for FAI (e.g., 995:1 for the 748-nm 1-km band compared to 157:1 for the 859-nm 250-m band, [Hu et al., 2012](#)), thus compensating for the reduction in resolution when detecting small *Sargassum* mats. While the disadvantage of AFAI is its saturation over bright targets such as clouds and strong sunglint (therefore leading to less data coverage), its advantage is relatively easy cloud-masking, making the resulting imagery simple to interpret even by a layperson. Such characteristics are particularly important for near real-time applications. One example of the AFAI imagery distributed online is shown in [Fig. 1](#). The *Sargassum* slicks can be clearly visualized after cloud-masking. In total, 17,772 MODIS AFAI images from Terra and Aqua measurements between April 2000 and November 2015 were generated in order to develop a time series, corresponding to about 95 images per month.

To help understand the observed *Sargassum* distribution patterns, environmental data were obtained from several sources. Three data types were obtained from NASA's Giovanni online visualization and analysis system (<http://giovanni.sci.gsfc.nasa.gov/giovanni/>). These data included: 1) cloud fraction data from the Atmospheric Infrared Sounder (AIRS) AIRX3STM v006 between January 2009 and October 2015; 2) precipitation data from the Tropical Rainfall Measuring Mission (TRMM) TRMM_3b43 v7 between January 2009 and August 2015; and 3) aerosol optical depth (AOD, 500 nm) data from the Ozone Monitoring Instrument (OMI) OMAERUVD v003 between January 2009 and November 2015. In addition to Giovanni data, sea surface temperature (SST) anomaly data were derived from National Oceanic and Atmospheric Administration (NOAA) Optimum Interpolation (OI) SST V2 monthly mean products (provided by the NOAA/OAR/ESRL PSD, Boulder, Colorado, USA, from their Web site at <http://www.esrl.noaa.gov/psd/>) from January 2009 to August 2015. Photosynthetically available radiation (PAR) data were obtained from the MODIS Aqua 4 km monthly mean products (<http://oceancolor.gsfc.nasa.gov/cgi/l3>) from January 2009 to August 2015. And finally, Amazon River discharge data were acquired from the Brazilian National Water Agency at station Obidos (<http://www2.ana.gov.br/Paginas/EN/default.aspx>). The station is located 800 km upstream from the Atlantic Ocean and is above the tide's influence thus normal water-discharge fluctuations can be detected.

4. Technical approach

Given the available 17,772 AFAI MODIS images, the process for mapping and quantifying the *Sargassum* distribution and coverage is composed of three major steps:

- 1) Classification of individual image pixels into three classes:
 - A) no-observation (this class includes no satellite coverage, sunglint, clouds, cloud shadows, and all other image artifacts);
 - B) *Sargassum*-free; and
 - C) *Sargassum*-containing.
- 2) Unmixing of the *Sargassum*-containing class using local thresholds for minimal (0%) and maximal (100%) sub-pixel coverage in order to estimate the fractional *Sargassum* coverage within a pixel.
- 3) Data binning of the individual image pixels into pre-defined grids at given time intervals (month, season, year) for the entire study

period (2000–2015), which leads to time series of area coverage and distribution maps.

Note that in reality the elevated AFAI signal can be from any floating vegetation, not just *Sargassum*. These floating vegetation include *Trichodesmium* mats ([Hu et al., 2010b](#); [Subramaniam, Brown, Hood, Carpenter, & Capone, 2002](#)). This is actually where the name of floating algae index came from ([Hu, 2009](#)). However, in the context of *Sargassum* mapping the elevated AFAI signal is deemed to come from *Sargassum* mats based on both direct and indirect evidence (see [Discussion](#)).

The entire process is summarized in the flowchart in [Fig. 2](#). Specifically, after masking clouds, sunglint and land, initial *Sargassum* pixel extraction is achieved by comparing the original AFAI image and a surface fitted image (generated by computing a four-degree polynomial fit to a surface with the valid AFAI pixels in each image). The extracted pixels are marked as potential *Sargassum*-containing pixels, and are excluded from the median filter used to calculate the *Sargassum*-free background ocean AFAI signal. The 'difference image' between the original AFAI image and background *Sargassum*-free ocean AFAI image is then segmented to extract the final *Sargassum*-containing pixels using a global scope (meaning within the CWA region in this work) threshold, T_0 . False-positives over cloud shadow pixels (e.g., [Fig. 1](#)) are masked as invalid data. For each *Sargassum*-containing pixel a linear unmixing scheme, based on locally-adjusted lower (0% sub-pixel) and upper (100% sub-pixel) bound coverage, is used to determine the fractional *Sargassum* coverage within a pixel. Finally, all valid pixels (both *Sargassum*-free and *Sargassum*-containing) within a pre-defined grid and a given time interval (month, season, year) are used to calculate the mean *Sargassum* fractional coverage for that grid and time interval. Statistical analyses of all grids lead to distribution and coverage maps. Below these steps are described in detail.

4.1. Step 1: Pixel classification into three classes: No observation (A), *Sargassum*-free (B), and *Sargassum*-containing (C)

4.1.1. No observation due to no satellite coverage, sunglint, clouds, or cloud shadows

All these conditions were treated as no observation, as no information on whether a pixel contains *Sargassum* can be determined.

4.1.1.1. No coverage. Each AFAI image was mapped to a rectangular projection, where some of the pixels in the projected image may not be covered by MODIS measurements. These pixels were assigned a value of -0.0999 during map projection. Pixels meeting the following criteria were identified as no satellite coverage:

$$R_{\text{rc}}(667) = -0.0999 \text{ or } R_{\text{rc}}(748) = -0.0999 \text{ or } R_{\text{rc}}(869) = -0.0999. \quad (2)$$

4.1.1.2. Sunglint and cloud-masking. Both sunglint and clouds lead to enhanced reflectance in all spectral bands. In this study, pixels meeting the following criteria were identified as sunglint or clouds:

$$R_{\text{rc}}(667) > 0.2 \text{ or } R_{\text{rc}}(748) > 0.2 \text{ or } R_{\text{rc}}(869) > 0.2. \quad (3)$$

The criteria were determined through trial and error. Although SeaDAS processing generates a standard CLDICE (clouds or ice) flag ([Patt et al., 2003](#)), a comparison between CLDICE and the threshold-based cloud-masking ([Fig. 3](#)) shows that CLDICE over-masked *Sargassum*-free pixels in some cases ([Fig. 3e](#)) while under-masked *Sargassum*-containing pixels in other cases ([Fig. 3h](#)). The former would reduce the number of valid observations while the latter would reduce the number of *Sargassum*-containing pixels, both leading to increased uncertainties in the *Sargassum* coverage estimation. Note that CLDICE

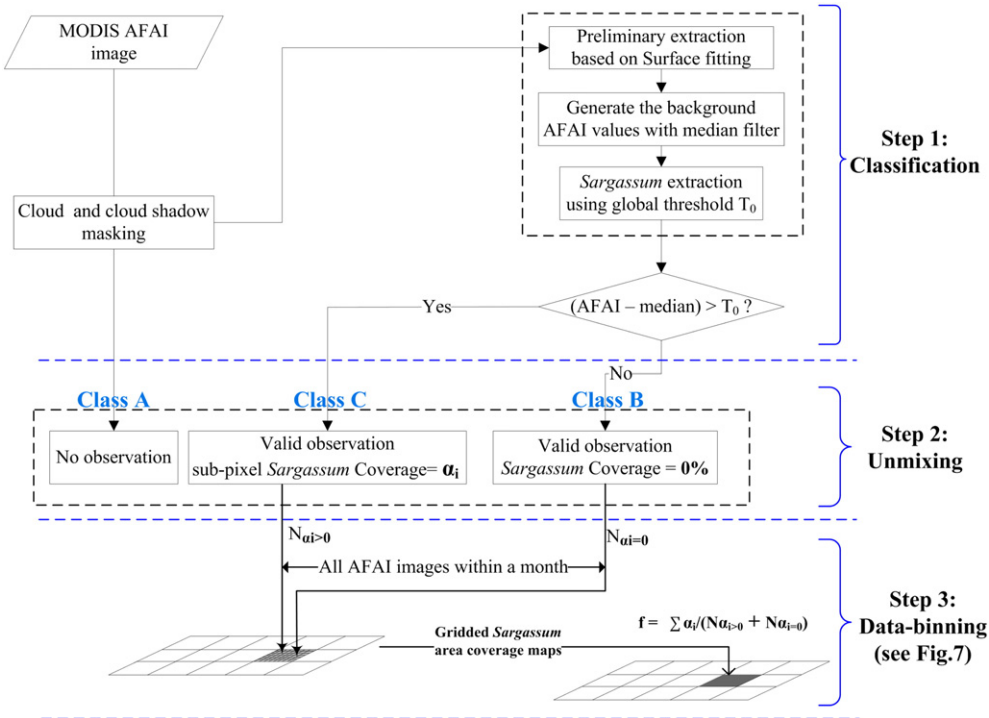


Fig. 2. Work flow to generate Sargassum distribution and coverage maps from MODIS AFAI images. They are generally grouped into three steps, as described in the text. Note that for simplicity and illustration purposes, cloud shadow masking is shown here as a preprocessing step before classification. Practically, cloud shadow masking has to rely on the preliminary classification results to improve the performance. Note that the illustration is to calculate a monthly mean, but the approach is the same for other time intervals. α_i represents the Sargassum subpixel coverage of the i th pixel. Details can be found in Section 4.1.1.

in SeaDAS was optimized for the processing of global ocean color data, with the ultimate goal of obtaining the highest-quality ocean color data products. In practice, to meet this goal CLDICE was determined in a conservative way, defined as $R_{rc}(859)$ (after subtracting an estimated sunglint reflectance) > 0.027 . This is why CLDICE masked many non-cloud pixels (including Sargassum-free water pixels and Sargassum-containing pixels). Furthermore, some of the sunglint pixels were not masked by CLDICE (gray-reddish color in Fig. 3), and these pixels have high AFAI values, leading to false positive detection. Because threshold-based cloud-masking avoided all these problems, this method was selected to mask both sunglint and clouds in this study.

4.1.1.3. Cloud shadow screening. Cloud shadow pixels show high AFAI values and may be falsely identified as Sargassum (see Fig. 4a & b)), leading to overestimation of the Sargassum area coverage.

Due to the lack of direct solar radiation, cloud shadow pixels show low R_{rc} values as compared with the surrounding pixels. In this study, a local total Rayleigh corrected reflectance (LTR) was first defined as

$$LTR = R_{rc}(469) + R_{rc}(555). \quad (4)$$

Then, the difference between LTR of the current pixel and a reference LTR value, defined as the mean LTR of a 31×31 pixel window centered at the current pixel, was examined. If the difference was lower than a predefined threshold, T_c :

$$LTR - Ref_{LTR} < T_c. \quad (5)$$

The current pixel was regarded as a cloud shadow pixel and masked as no observation. This cloud shadow masking is termed as local low

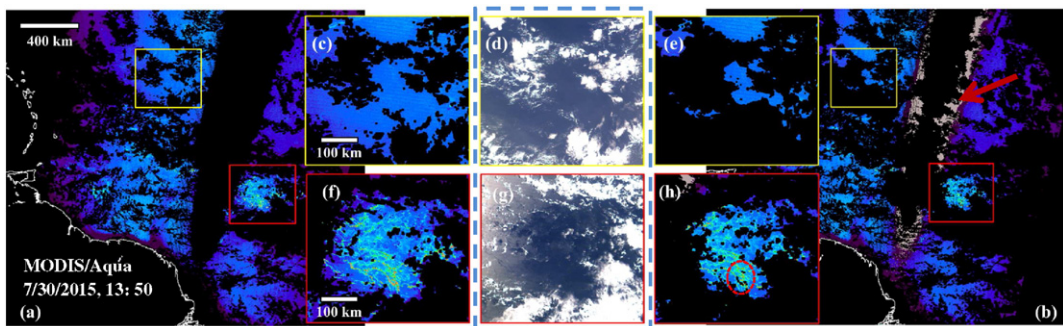


Fig. 3. Comparison between the threshold-based sunglint and cloud-masking (this study, (a)) and SeaDAS CLDICE masking (b). (c) and (f) are the enlarged regions from (a); (e) and (h) are the enlarged regions from (b); (d) and (g) are the corresponding RGB images to facilitate interpretation. CLDICE over-masked water pixels in (e) and Sargassum pixels in (h) (red dashed circle). The color legend of the AFAI images is the same as the one in Fig. 1.

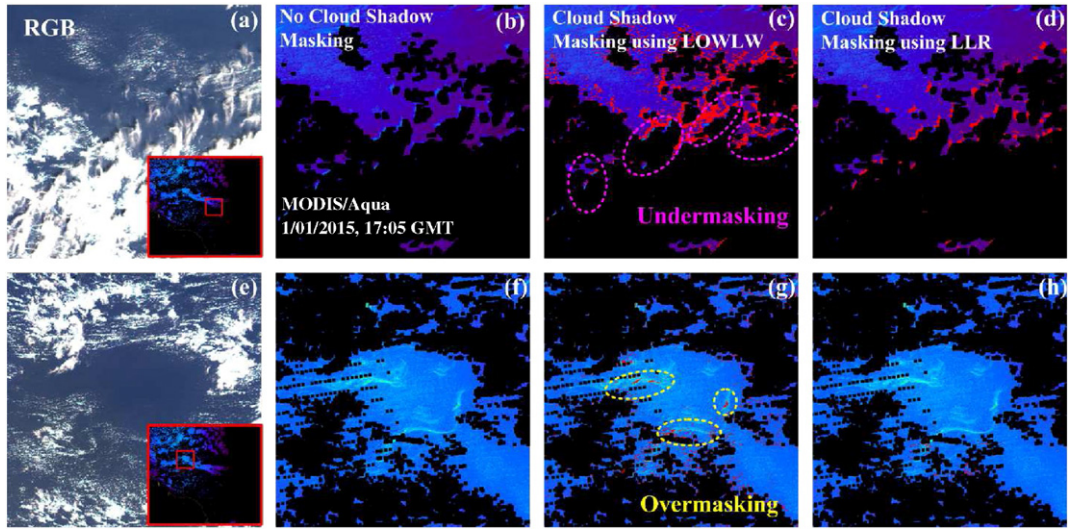


Fig. 4. Comparison between SeaDAS LOWLW and the LLR cloud shadow masking (this study). (a) and (e) are the enlarged RGB images; (b) and (f) are the unmasked AFAI images; (c) and (g) show the LOWLW flagged pixels in red; (d) and (h) show the LLR masked pixels (this study) in red. In (c), some of the cloud shadow pixels are missed by the LOWLW flag (pink circles). In (g), some of the *Sargassum*-containing pixels are flagged as cloud shadows (yellow circles).

reflectance (LLR) masking, where T_c was determined to be -0.01 after trial and error and a sensitivity analysis.

Ideally, a cloud shadow mask should retain most *Sargassum* pixels and exclude most cloud shadow pixels. To select the optimal T_c in the LLR cloud shadow masking, we manually delineated several regions of interest for cloud shadow pixels ($N_c = 2573$) and *Sargassum* pixels ($N_s = 49.559$). According to the cumulative and normalized histograms (Fig. 5a & b), a selection of $T_c = -0.01$ served this purpose. Therefore, $T_c = -0.01$ was used as the threshold to detect and mask cloud shadow pixels.

Note that the LOWLW flag generated by SeaDAS processing has also been proposed to detect cloud shadows (Patt et al., 2003). It is based on a threshold of $0.15 \text{ mW cm}^{-2} \text{ um}^{-1} \text{ sr}^{-1}$ in the derived normalized water-leaving radiance at 555 nm. However, a comparison between the LOWLW and LLR in Fig. 4 shows that LOWLW often missed some cloud shadow pixels (pink circles in Fig. 4c) while over-masked *Sargassum*-containing pixels (yellow circles in Fig. 4g). In contrast, both the under-masking of water pixels and the over-masking of *Sargassum*-containing pixels are reduced by the LLR cloud shadow masking method (Fig. 4).

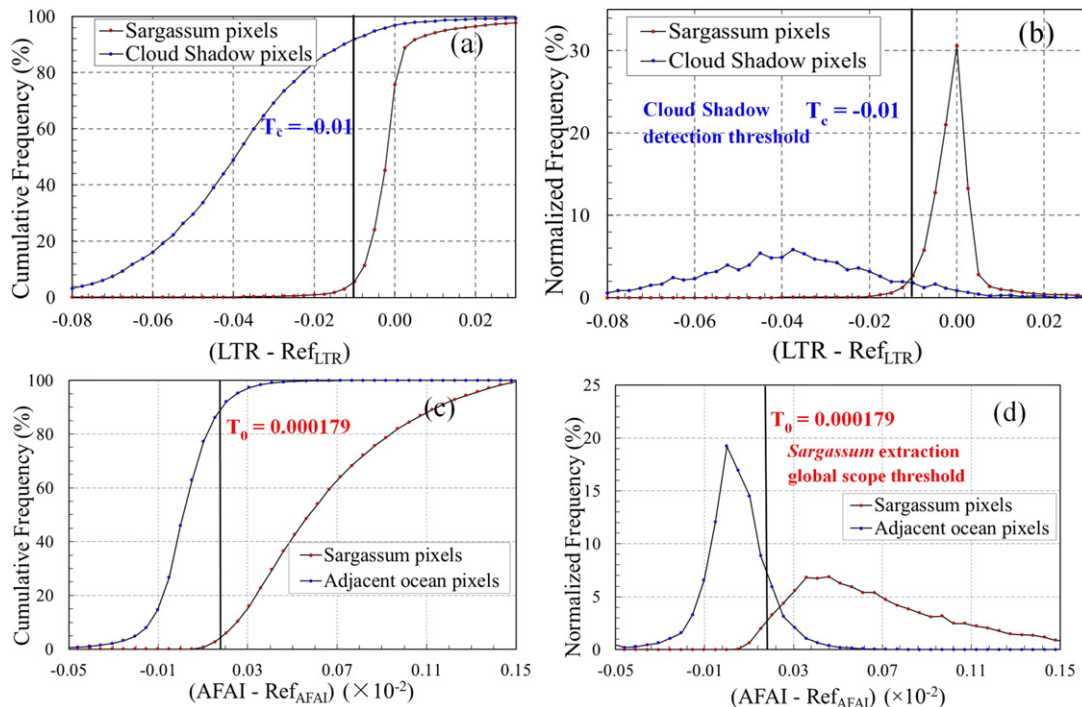


Fig. 5. Cumulative and normalized frequency distributions of *Sargassum* pixels, cloud shadow pixels and adjacent ocean pixels in several regions of interest. (a) and (b) show the distribution of the $(\text{LTR} - \text{Ref}_{\text{LTR}})$ values of *Sargassum* pixels and cloud shadow pixels. (c) and (d) show the distribution of the $(\text{AFAI} - \text{Ref}_{\text{AFAI}})$ values of *Sargassum* pixels and adjacent ocean pixels.

4.1.2. Class B and Class C: Sargassum-free and Sargassum-containing pixels

Due to the presence of sunglint contaminated pixels (adjacent to sunglint masked pixels), the relatively large swath of MODIS, and incomplete atmospheric correction, there are large-scale gradient differences across AFAI images (e.g., Figs. 1 & 3) where AFAI values over Sargassum-free water are lower near the satellite scan edge than around the scan center. This makes it impossible to apply a global scope threshold to extract Sargassum-containing pixels in uncorrected images. Several steps were used to account for this across-image gradient, which are described below. Basically, a median filter (after excluding potential Sargassum-containing pixels determined first from surface fitting) was used to generate a background Sargassum-free AFAI image, which was then subtracted from the original AFAI image. Then, a global scope image based threshold was determined and applied to the entire image to extract the Sargassum-containing pixels.

4.1.2.1. Preliminary Sargassum pixel extraction based on surface fitting. To model the large-scale variability, a four-degree surface fitting is usually sufficient. Higher-degree surface fitting is likely to cause overfitting, which will hinder the extraction of local bright targets (i.e., Sargassum-containing pixels). The surface fitting was performed over pixels of valid observations only, with Sargassum-containing pixels excluded. Because nearshore pixels tend to have high AFAI values, these pixels were also excluded before surface fitting. Pixels with AFAI values greater than the fitted value by a threshold T_s were identified as potential Sargassum-containing pixels, and were excluded from the median filter creation process used to determine the Sargassum-free ocean background.

The threshold T_s in the above process was determined from 8 representative AFAI images (4 in January and 4 in June). The Sargassum pixels were first manually delineated from the 8 images, which were then eroded using a 5×5 pixel window to assure the exclusion of Sargassum-containing pixels when creating the median filter. A threshold of $T_s = 2.55 \times 10^{-4}$ was found to extract up to 95% of the Sargassum-containing pixels (after erosion), and therefore was used for the entire dataset. Fig. 6a and d show the original AFAI image and resultant surface fitted image.

4.1.2.2. Median filtering to determine ocean background (Ref_{AFAI}). The surface fitting derived background image still contains small-scale variance, therefore requiring a subsequent median filter to refine the background image. The median filter used a 51×51 pixel window to determine the median value of each pixel from the surface fitted image. This derived median image was used as the Sargassum-free ocean background, Ref_{AFAI} , to extract Sargassum-containing pixels by using a global scope threshold, T_0 .

Adopting the use of a 51×51 pixel window ($W_{\text{size}} = 51$ pixels) was based on several considerations. Because large Sargassum slicks do occur, a minimum W_{size} of 31 pixels could be used to fill in the surface fitting derived bright targets to avoid data loss. In Garcia et al. (2013) the optimal W_{size} was obtained by comparing the standard error of the means (SEMs) from 10 randomly selected ocean regions. The SEMs would increase in a nonlinear fashion when W_{size} exceeded a certain value. In this study, randomly selected ocean regions within the CWA region from 6 representative images were analyzed to determine an optimal W_{size} . The SEMs of these selected ocean regions only decreased slowly with decreasing W_{size} when W_{size} was < 51 . This suggested that after excluding potential Sargassum-containing pixels from the surface fitting process, a median filter could be used effectively to remove small-scale variations providing a large-scale Sargassum-free ocean background (Ref_{AFAI} , Fig. 6g). Considering the typical size of the potential Sargassum slicks and computational efficiency, $W_{\text{size}} = 51$ was selected for use in the median filter.

4.1.2.3. Final Sargassum pixel extraction using a global scope segmentation threshold T_0 . With the Sargassum-free ocean background (Ref_{AFAI}) obtained from the two processes above, a global scope threshold T_0 was determined and applied to the entire image to extract the Sargassum-containing pixels whose AFAI values were higher than the background values of T_0 :

$$\text{AFAI} - \text{Ref}_{\text{AFAI}} > T_0. \quad (6)$$

T_0 was determined by comparing the cumulative frequency of manually delineated Sargassum-containing pixels and their adjacent pixels with a dilation of 5 pixels (11×11 pixel window). The dataset used to

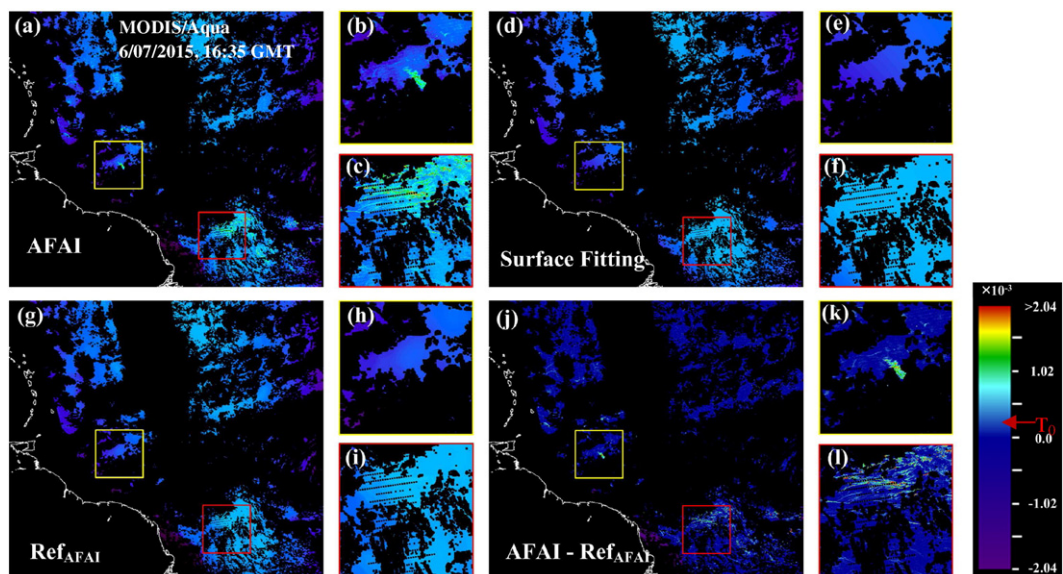


Fig. 6. An example of the Sargassum pixel extraction process. (a) is the original AFAI image after masking sun glint, clouds, cloud shadows, and land; (b) and (c) are enlarged regions from the AFAI image in (a); (d) is the surface fitted image from (a); (e) and (f) are enlarged regions from the surface fitted image in (d); (g) is the median-filtered (Ref_{AFAI}) image that is used as the reference; (h) and (i) are the enlarged regions from the Ref_{AFAI} image in (g); (j) is the difference image between (a) and (g); (k) and (l) are the enlarged regions from the AFAI- Ref_{AFAI} (difference) image in (j). Sargassum-containing pixels are extracted from the difference image using the global scope threshold T_0 . The color bar is for the difference image and the red arrow marked the global scope threshold T_0 used in this study.

determine T_0 was the same as that used to determine the surface fitting threshold. The logic was also the same: T_0 should preserve most of the manually selected “ground truth” Sargassum-containing pixels while excluding most of the adjacent Sargassum-free pixels. As marked by the vertical line in the cumulative frequency distribution (Fig. 5c), when T_0 was selected to be 1.79×10^{-4} , about 95% of the Sargassum-containing pixels were captured while only 10% of the adjacent Sargassum-free pixels were misclassified as Sargassum-containing. As with any threshold-based method, the choice of the threshold is always a compromise between false-positive and false-negative detections. The sensitivity test below shows that $T_0 = 1.79 \times 10^{-4}$ would lead to acceptable uncertainties in both categories, and would not impact the overall findings in the long-term trend of Sargassum distributions.

To understand the uncertainties in the extraction results, 12 representative MODIS AFAI images (6 from January 2015 and 6 from June 2015), all independent from the dataset used in determining T_0 , were used to extract Sargassum-containing pixels following the above procedures, with their results compared to those with manual delineation (regarded as the “truth”). For the estimates of Sargassum area coverage using unweighted Sargassum-containing pixels, the false positive rate was 30.41% and the false negative rate was 15.67%. Due to these uncertainties, a linear unmixing method was developed (see below) and applied to Sargassum-containing pixels. After weighting the Sargassum-containing pixels using this linear unmixing method, the false positive rate decreased to 18.97% and the false negative rate decreased to 7.42%. As shown in Table 1, the overall accuracy, defined by the F-score (Chinchor & Sundheim, 1993) was 86.05%, and thus acceptable for time series and trend analysis.

4.2. Step 2: Unmixing of Sargassum-containing pixels to determine fractional coverage (>0% but ≤100%)

So far, for every AFAI image, each pixel was classified as no-observation (Class A), Sargassum-free (Class B), or Sargassum-containing (Class C). For the Sargassum-containing pixels, the next step is required to determine the fractional coverage through unmixing, as Sargassum mats can rarely occupy the entire 1-km pixel. This linear unmixing scheme is used to quantify the percentage of Sargassum coverage within a given pixel. For each Sargassum-containing pixel, its fractional coverage was determined as

$$\text{AFAI}_U = \text{AFAI}_{U0} - (\text{AFAI}_{L0} - \text{AFAI}_L) \quad (7)$$

$$\alpha_i = (\text{AFAI}_{Ai} - \text{AFAI}_{Li}) / (\text{AFAI}_{Ui} - \text{AFAI}_{Li}) \times 100\%. \quad (8)$$

where α_i is the fractional (percentage) Sargassum coverage (ranging from 0.0% to 100.0%) for the i th Sargassum-containing pixel, AFAI_{Ai} is the AFAI value of the i th Sargassum-containing pixel (“A” in the subscript represents “algae”, i.e., Sargassum), AFAI_{Li} and AFAI_{Ui} are the lower (corresponding to 0.0% coverage) and upper (corresponding to 100.0% coverage) bounds for the i th Sargassum-containing pixel, respectively. AFAI_{L0} and AFAI_{U0} are the global scope lower and upper bounds (image and pixel independent constants) for 0% and 100% sub-pixel coverage, respectively. AFAI_L and AFAI_U are the local lower and upper bounds, respectively, for the Sargassum patch containing the i th Sargassum-containing pixel, which may vary among Sargassum patches and images. Therefore, to determine α_i , four parameters are required: AFAI_{U0} , AFAI_{L0} , AFAI_U , and AFAI_L .

To determine AFAI_{U0} , which represents 100% Sargassum coverage within a pixel, surface reflectance measured from pure Sargassum mats in the GOM and off Bermuda (Fig. 1b) were used to simulate R_{rc} and AFAI as sensed by MODIS through radiative transfer simulations. The collection of these spectra was described in Hu et al. (2015). The simulation is the same as described in Hu (2009):

$$R_{rc} = R_a + t_o T R_{sarg} \quad (9)$$

where R_a is the atmospheric path reflectance due to aerosols and aerosol-Rayleigh interactions, R_{sarg} is the mean Sargassum reflectance from field measurements (Fig. 1b), t_o is the atmospheric diffuse transmittance from the sun to the Sargassum mat, and T is the atmospheric beam transmittance from the Sargassum mat to the satellite sensor. Because of the atmospheric effects, the same R_{sarg} could result in different R_{rc} as measured by the satellite. Such effects were simulated in the following way.

Two solar/viewing scenarios were considered in the simulation, with one for image center and the other for image edge. Two aerosol types were considered: maritime aerosols with 90% relative humidity (m90) and coastal aerosols with 50% relative humidity (c50), representing both open ocean and coastal ocean scenarios. Aerosol optical thickness at 869 nm, $\tau_a(869)$, was varied between 0.02 and 0.38 (the upper bound for aerosols, Robinson, Franz, Patt, Bailey, & Werdell, 2003). All variables in Eq. (9) (i.e., R_a , t_o , T) corresponding to these different scenarios were determined using the MODIS aerosol lookup tables from the SeaDAS data processing software package (Baith, Lindsay, Fu, & McClain, 2001). Table 2 presents a summary of the MODIS AFAI_{U0} values corresponding to all variable atmospheric conditions and solar/viewing geometry. The 2013–2015 climatological mean $\tau_a(869)$ for the CWA region was estimated to be 0.10. The mean value corresponding to $\tau_a(869) = 0.10$, 4.41×10^{-2} , was used in this study to represent the global AFAI_{U0} for 100% Sargassum coverage within a pixel. Note that for an individual Sargassum slick, the local upper bound was adjusted using Eq. (7) to account for variable atmospheric and observing conditions.

To determine AFAI_{L0} , a histogram of AFAI values from all water pixels near these Sargassum slicks (6 pixels outward from the slick edges) was generated. The median value was determined to be -8.77×10^{-4} and was assigned to AFAI_{L0} to represent 0% Sargassum-containing coverage. Here the median value is selected to avoid noise interference in calculating the lower bound. For each Sargassum patch, the local AFAI_L was also determined using the same method. The local AFAI_U was derived using Eq. (7) by normalizing the global AFAI_{U0} against the difference between AFAI_{L0} and AFAI_L . These values were then used in Eq. (8) to calculate sub-pixel coverage α_i for each of the Sargassum-containing pixels within a Sargassum patch. This method was applied in a loop through all Sargassum patches within an image. Fig. 7a, b, c, and d show an example of the process for extracting Sargassum-containing pixels and determination of sub-pixel coverage.

4.3. Step 3: Data binning to derive distribution and area coverage maps

After obtaining the sub-pixel coverage of each Sargassum-containing pixel from all images, the entire study region was divided into $0.5^\circ \times 0.5^\circ$ grids to generate mean distribution maps at different time intervals (monthly, seasonal, and annual). For each grid, mean fractional Sargassum coverage within a particular time interval was calculated

Table 1
Uncertainty and accuracy assessment of the final Sargassum-containing pixel extraction using sample images in January and June 2015.

	False positive	False negative	Precision	Recall	F score
Area coverage using unweighted Sargassum pixels (AUP)	30.41%	15.67%	72.80%	81.38%	76.85%
Area coverage using weighted Sargassum pixels (AWP)	18.97%	7.42%	82.57%	89.84%	86.05%

Table 2

MODIS AFAI upper bound values (i.e., corresponding to 100% Sargassum coverage within a pixel) for various atmospheric conditions (aerosol type and optical thickness) and solar/viewing geometry, based on Eq. (9) and radiative transfer simulations.

m90	$\tau_a(869)$									
	0.02	0.06	0.10	0.14	0.18	0.22	0.26	0.30	0.34	0.38
$\theta = 4^\circ$	0.052	0.050	0.048	0.045	0.043	0.041	0.040	0.038	0.036	0.034
$\theta = 57^\circ$	0.049	0.046	0.042	0.039	0.036	0.033	0.030	0.028	0.026	0.024
c50	$\tau_a(869)$									
	0.02	0.06	0.10	0.14	0.18	0.22	0.26	0.30	0.34	0.38
$\theta = 4^\circ$	0.052	0.049	0.046	0.044	0.042	0.039	0.037	0.035	0.033	0.031
$\theta = 57^\circ$	0.049	0.045	0.041	0.037	0.033	0.030	0.027	0.025	0.022	0.020

Note: Two aerosol types are selected for open and coastal oceans: maritime aerosols with 90% relative humidity (m90) and coastal aerosols with 50% relative humidity (c50). Two solar/viewing scenarios are applied: near satellite nadir (satellite zenith $\theta = 4^\circ$, solar zenith $\theta_0 = 18.4^\circ$, relative azimuth $\phi = 22^\circ$) and near scan edge ($\theta = 57^\circ$, $\theta_0 = 29^\circ$, $\phi = 21^\circ$). $\tau_a(869) = 0.10$ corresponds to the mean aerosol optical thickness over the study region between 2013 and 2015 as derived from MODIS. The average of these values for $\tau_a(869) = 0.10$ is 4.41×10^{-2} , (bold font), which was used in this study as the global upper bound for pure Sargassum coverage.

from all Sargassum-containing (N_A) and Sargassum-free pixels (N_W) falling in that grid as

$$f = \frac{1}{N} \left[\sum_{i=0}^N \alpha_i \right] \quad (10)$$

$$N = N_A + N_W \quad (11)$$

where the summation was for all Sargassum-containing and Sargassum-free (i.e., water) pixels in that grid within the time interval, with $\alpha_i = 0.0$ for water pixels. The mean area coverage maps were generated after integrating all grids. The general process is illustrated in Fig. 7.

5. Results: Long-term Sargassum distribution and coverage

The above methods were applied to the entire time series between 2000 and 2015, where 17,772 MODIS AFAI images (9013 between 2009 and 2015) were used to generate the Sargassum distribution and coverage maps over the CWA region at monthly, seasonal, and annual intervals. The threshold values were selected as: $T_0 = 1.79 \times 10^{-4}$, $AFAI_{U0} = 4.41 \times 10^{-2}$, and $AFAI_{L0} = -8.77 \times 10^{-4}$.

Fig. 8 presents the distributions of monthly mean coverage of Sargassum in the study region between 2000 and 2015. The color-coded value represents the monthly mean percentage of Sargassum coverage for a

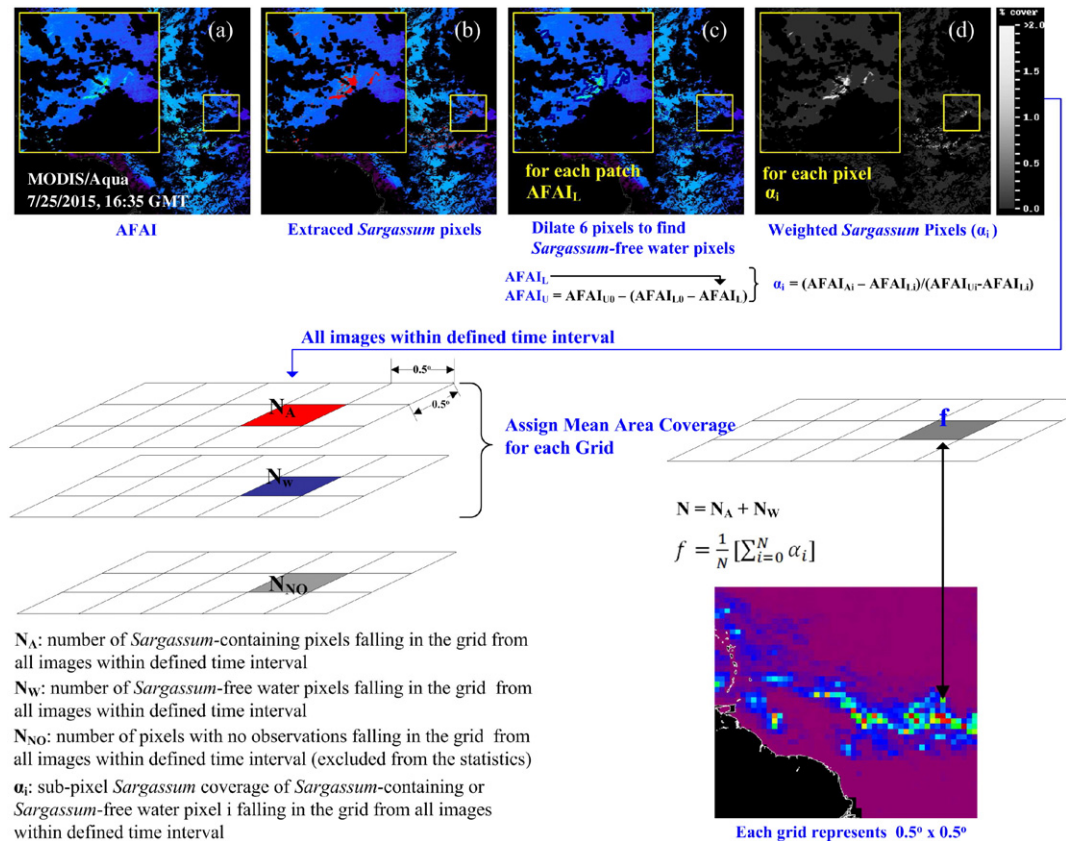
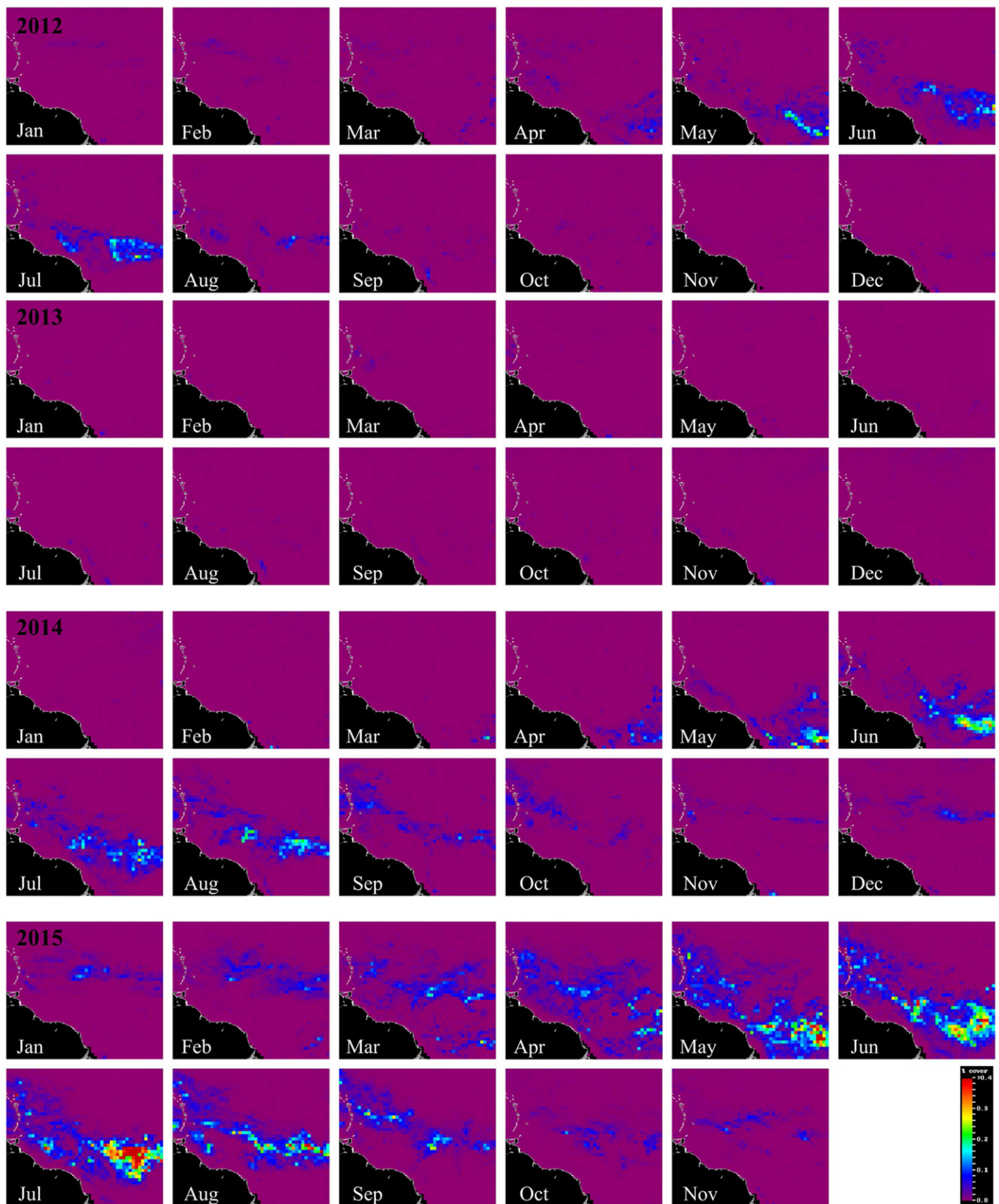


Fig. 7. The process used to generate the monthly mean Sargassum area coverage maps using original AFAI images. The AFAI image in (a) is used to extract Sargassum-containing pixels in (b). These pixels are dilated to find the nearest water pixels (dark blue color around the Sargassum patches in (c)) to be used to calculate $AFAI_L$ for each Sargassum patch. (b) and (c) are used to calculate (d), the required input to generate monthly means for the predefined grids. The calculation of the mean Sargassum coverage for a grid during the time interval month is illustrated.



Fig. 8. Monthly mean distribution maps show *Sargassum* area coverage in the CWA region between 2000 and 2015, derived from MODIS AFAI images using the approach developed in this paper. Land is masked to black and coastline is masked to white. The November monthly mean in 2015 contains data up to 21 November 2015. Because the results for 2000–2009 are very similar (and they all show minimal *Sargassum* coverage), for clarity the distribution maps between 2001 and 2008 are omitted.

**Fig. 8** (continued).

given grid, varying from 0% to about 0.4%. Because the results for 2000 through 2009 are very similar and they all show minimal *Sargassum* coverage, for clarity the distribution maps between 2001 and 2008 are

omitted here. During that period, small numbers of *Sargassum* slicks occasionally appeared off the Amazon River mouth between August and October, and the daily time sequence indicated northward movement.

Table 3

Annual mean *Sargassum* coverage over the CWA region between 2009 and 2015. The annual mean coverage between 2000 and 2008 was similar to those in 2009, thus not listed in the table.

Year	2009	2010	2011	2012	2013	2014	2015
Mean fractional coverage (%)	0.02	0.03	0.07	0.08	0.02	0.12	0.32
Mean area coverage (km ²)	59.6	83.5	199.5	232.1	66.5	375.1	956.2

However, they did not develop into large-scale blooms during those periods.

Large amounts of *Sargassum* slicks did not appear until April 2011 when they were captured in MODIS AFAI imagery around 3.0° N and 40° W. These *Sargassum* slicks then developed and advected to the Lesser Antilles Islands in the southern Caribbean from May to July. This agrees well with the timing of the reported *Sargassum* beaching events in those islands. From August to September, massive *Sargassum* slicks started to decrease. Some *Sargassum* slicks still appeared off the Amazon River mouth later in October and November, but their sizes were much smaller.

In 2012, *Sargassum* distribution patterns closely resembled those found in 2011 except for the scattered slicks in the first months of 2012 around 18°N which were apparently left over from the 2011 bloom. During July, most of *Sargassum* slicks appeared between 5°N and 10°N. Unlike 2011, August 2012 experienced a significant decrease of the total *Sargassum* coverage, after which only small amounts of scattered *Sargassum* slicks were found off the Amazon River mouth.

One interesting result is that after September 2012 and for the entire year of 2013, very few *Sargassum* slicks were found until April 2014, after which *Sargassum* distribution patterns nearly repeated those found during the summers of 2011 and 2012 but with greater abundance. The difference between 2014 and these two previous years is that between September and December 2014, there were still considerable numbers of *Sargassum* slicks, which continued to appear through the early months of 2015.

The most striking result was found in the extremely anomalous year of 2015. Not only did the *Sargassum* slicks appear from the very beginning of the year – which were again, apparently, left over from the previous year's bloom, but the *Sargassum* coverage during the spring and summer months was much greater than in any previous year. As of October and November of 2015, there were still considerable amounts of *Sargassum* in the offshore waters. This is analogous to conditions found in the same months of 2014, thus posing the question of whether similar extreme *Sargassum* blooms may occur in 2016.

The same method was used to generate seasonal and annual mean distribution maps. From these maps, the total area coverage was calculated to integrate *Sargassum* mean area coverage from all grids. While

Table 3 presents a summary of the integrated annual mean area coverage between 2009 and 2015, Fig. 9 shows the time series of the integrated monthly and seasonal mean coverage. These statistics provide a quantitative measure of the amount of *Sargassum* in the CWA region at monthly, seasonal, and annual scales. The distribution maps in Fig. 8 closely resemble the time series which clearly shows the anomalous years of 2011, 2012, 2014, and 2015. Most striking is that 2015 is an extreme year when both the annual mean coverage and summer mean coverage were 4 times of those found in 2011, and the summer mean coverage exceeded those in the pre-bloom years (2009 and 2010) by 20 times.

6. Discussion

While this is the first time that long-term *Sargassum* distribution maps and coverage statistics are presented by applying a sophisticated but objective methodology to MODIS observations, two questions naturally arise from these results. The first is how much can they be trusted? The second is, if they are trusted, what caused these long-term patterns? Due to the lack of field measurements, neither is easy to address. However, from spectral analysis, sensitivity analysis, and the analysis of several environmental variables, the following discussion may provide some useful hints.

6.1. Sargassum or other floating materials?

From the perspective of spectroscopy, it is difficult to conclude that the observed red-edge reflectance (i.e., elevated AFAI values) is due to *Sargassum* instead of other floating vegetation. Using multi-sensor data and simulations, Hu et al. (2015) suggested that unless hyperspectral data are used, it is very difficult to differentiate *Sargassum* from other floating vegetation, as the latter also show elevated AFAI values. This is particularly true when the sub-pixel coverage is very small (<25%). Therefore, currently there is no way to validate all observed slicks from the AFAI imagery. However, two facts can help confirm that the observed slicks are mostly, if not all, *Sargassum*.

The first is scarce validation using the Hyperspectral Imager for the Coastal Ocean (HICO) observations. Hu et al. (2015) showed that corresponding to some of the MODIS-observed slicks, HICO spectra of the same slicks showed diagnostic spectral curvature around 630 nm due to chlorophyll c absorption. This is a unique feature for *Sargassum* macroalgae, thus confirming that at least some of the slicks observed from the MODIS AFAI imagery are indeed *Sargassum*. Likewise, the spectral curvature between reflectance of blue and green bands (Hu et al., 2010b) from randomly selected dense slicks (high AFAI values) did not reveal spectral characteristics of *Trichodesmium* mats, confirming that at least these randomly selected dense slicks were not *Trichodesmium* but likely *Sargassum*.

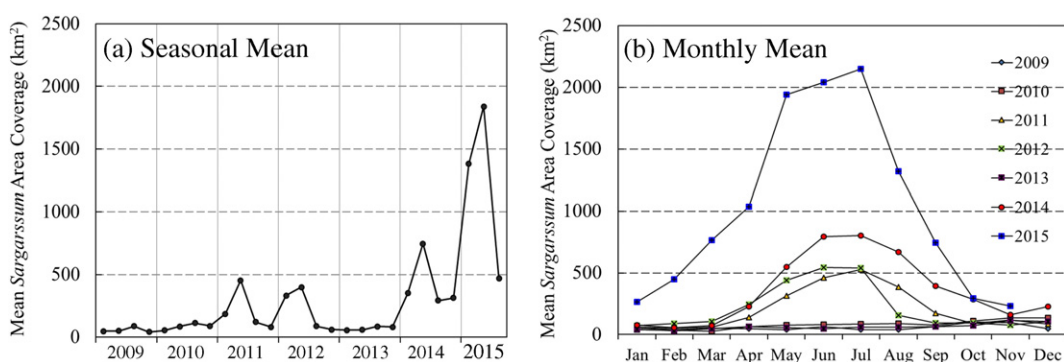


Fig. 9. Mean *Sargassum* area coverage at seasonal (a) and monthly (b) scales between 2009 and 2015 for the CWA region. The statistics between 2000 and 2008 are similar to those in 2009 and 2010, and thus omitted.

Local news reports from the Lesser Antilles Islands provide another indirect source of evidence. In 2011, 2012, 2014, and 2015, there were numerous new reports of *Sargassum* beaching on these islands, supporting the findings here. In particular, the news exposure increased tremendously in 2015, also supporting the statistical results that show 2015 as an extreme year.

Given the direct and indirect evidences, it is believed that most of these observed slicks, if not all, are *Sargassum* macroalgae. However, this does not mean that a field survey is not needed to further validate the observations here, particularly when area coverage estimations are to be made.

6.2. Uncertainties in the estimation of mean *Sargassum* area coverage

6.2.1. Sensitivity analysis

Several thresholds were used throughout the entire process to derive the final mean area coverage maps, which included T_c in the LLR cloud shadow masking, the global scope segmentation threshold T_0 to determine *Sargassum*-containing pixels, and $AFAI_{U0}$ and $AFAI_{L0}$ to determine sub-pixel *Sargassum* coverage. To understand the sensitivity of the final results to changes in these threshold values, a total of 187 AFAI images from MODIS Aqua and Terra in January and June 2015 were selected to generate the monthly mean area coverage maps with different combinations of variable threshold values.

Fig. 10a shows the comparison between the three choices for cloud shadow determination: no masking, LLR masking (this study), and cloud-edge dilation (6 pixels) masking. The global scope $AFAI_{U0}$ and $AFAI_{L0}$ were set as the default (4.41×10^{-2} and -8.77×10^{-4}). Compared to a proper masking method, no masking led to overestimated total *Sargassum* area coverage because some of the cloud shadow pixels were misclassified as *Sargassum*. The dilation-based cloud-masking method overestimated total *Sargassum* coverage even more because

the total number of valid observations (N in Eq. (11)) was significantly reduced in June when large *Sargassum* coverage appeared. Indeed, a 6-pixel dilation led to up to 60% of data loss of total number of valid observations from individual images in this analysis.

To assess the effect of T_0 on the estimation of mean *Sargassum* area coverage, T_0 was varied between 1.28×10^{-4} and 2.55×10^{-4} , with mean *Sargassum* area coverage estimated for each T_0 (**Fig. 10b**). As expected, the estimated mean area coverage decreased with increasing T_0 . For June 2015, the mean *Sargassum* area coverage decreased by ~10% when T_0 was changed from 1.53×10^{-4} to 1.79×10^{-4} . A ~19% percentage decrease was observed for January of 2015. However, while the absolute area coverage changed with T_0 , the seasonal and long-term patterns remained stable.

The estimates of monthly mean *Sargassum* area coverage were also sensitive to changes in $AFAI_{L0}$ and $AFAI_{U0}$. When $AFAI_{L0}$ was varied, $AFAI_{U0}$ was set to be the default value (4.41×10^{-2}). When $AFAI_{U0}$ was varied, $AFAI_{L0}$ was set to be the default value (-8.77×10^{-4}). **Fig. 10c** shows that when $AFAI_{L0}$ is increased, the mean *Sargassum* area coverage for January and June 2015 both increased slightly. Increasing the low bound from -8.77×10^{-4} to 6.21×10^{-4} results in larger estimation of ~0.57% for June 2015. As expected, **Fig. 10d** shows that when $AFAI_{U0}$ was increased, the mean area coverage for January and June 2015 also decreased. Similarly, an increase of the $AFAI_{U0}$ bound from 4.414×10^{-2} to 4.440×10^{-2} leads to a 0.44% decrease in the mean area coverage in June 2015. Since the range between $AFAI_{U0}$ and $AFAI_{L0}$ is up to $\sim 4.4 \times 10^{-2}$, adjustment of the $AFAI_{U0}$ and $AFAI_{L0}$ at scale of 1×10^{-4} will both result in minimal changes.

Although the absolute value of the area coverage changes with these changing threshold values, the relative long-term patterns are insensitive to changes in the thresholds. For example (**Fig. 11**) shows T_0 varying from 1.28×10^{-4} to 2.30×10^{-4} , while the monthly mean area

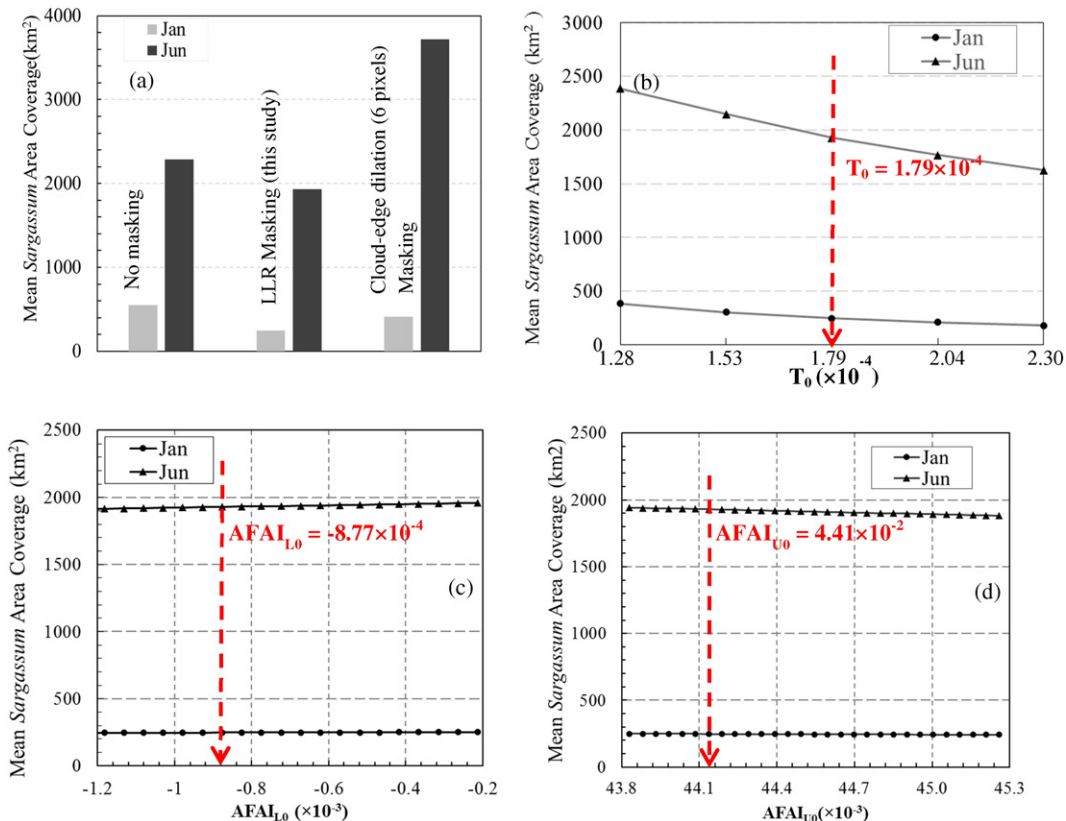


Fig. 10. Sensitivity of mean *Sargassum* area coverage (km²) in January and June 2015 to different cloud shadow masking methods (a), different segmentation thresholds (b), different lower and upper bounds (c and d). The red dashed lines indicate the threshold values selected in this study for time series analysis.

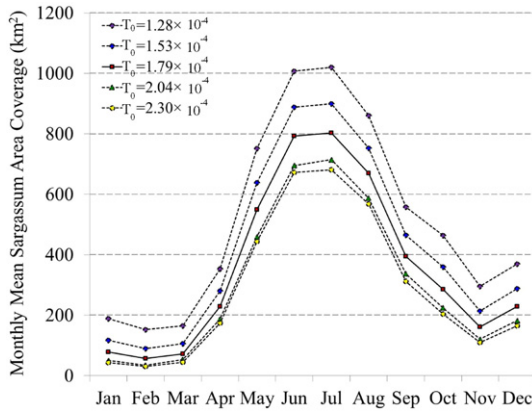


Fig. 11. Monthly mean *Sargassum* area coverage during 2014 generated with different global scope threshold T_0 . In this study, $T_0 = 1.79 \times 10^{-4}$ was selected to generate time-series statistics.

coverage decreased in all months of 2014, the temporal patterns remained nearly identical. Furthermore, the absolute area coverage appeared less sensitive to T_0 when T_0 was 1.79×10^{-4} . Therefore, a T_0 of 1.79×10^{-4} was selected in this study. In the future, field-based measurements may be used to help determine this threshold. At present, the results presented here represent the best knowledge one can obtain from MODIS observations and, even in the worst-case scenario, the relative temporal patterns as well as the distribution maps still remain valid.

6.2.2. Detection limit

The MODIS pixels used in this study have a ground resolution of 1 km, making it difficult to observe small *Sargassum* rafts. Using simulations and assuming 200:1 SNR, Hu et al. (2015) suggested that the lower detection limit of the red-edge reflectance is about 1–2% of a pixel size. However, the MODIS band used in examining the red-edge reflectance, the 748-nm band, has a SNR of 995:1 (Hu et al., 2012) under typical conditions. This would certainly enable MODIS AFAI to detect *Sargassum* rafts smaller than 1% of a pixel size. Manual analysis of delineated AFAI slicks with weak signals indicated that the detectable limit would be ~0.2% of a MODIS 1-km pixel. This is 5 times more sensitive than the estimates from the 200:1 SNR assumption. Correspondingly, a *Sargassum* raft with an effective width of >2 m and effective length of >2 km long is observable in MODIS AFAI imagery. Smaller *Sargassum* rafts are simply not observable.

6.2.3. Uncertainties due to non-optimal observing conditions

Many factors can impact satellite observations of surface slicks of *Sargassum*. For near real-time observations, clouds, severe sun glint, cloud shadows, and other artifacts simply make many pixels unusable, presenting a major hurdle for near real-time *Sargassum* tracking. However, these pixels are not counted in long-term statistics, thus would have minimal impacts on the statistical results once sufficient number of images is used in the statistics. On the other hand, non-optimal observing conditions such as variable winds and currents may have significant impacts on the statistical results (Gower & King, 2011; Marmorino, Miller, Smith, & Bowles, 2011; Szekielda, Marmorino, Bowles, & Gillis, 2010; Woodcock, 1993). Under high winds, *Sargassum* may be dissipated and become undetectable to MODIS imagery while they may still be observed in high-resolution airborne imagery or field sampling through neuston net tows. Attempts were made to determine the optimal wind range from sequential images, however mixed results were obtained. When wind speed was $>7 \text{ m s}^{-1}$, *Sargassum* tended to be undetectable in MODIS imagery. However, this threshold could not be generalized, and therefore was not applied to screen data. In this sense, because *Sargassum* aggregate or mat size is important to *Sargassum* coverage or biomass estimates (Dierssen et al., 2015), the results obtained here are

likely underestimates and they represent only those *Sargassum* slicks observable by MODIS. In other words, the absolute area coverage values represent lower bound of *Sargassum* coverage. Regardless, the lack of significant inter-annual variability or wind speed trends suggests that wind should not impact the observed distribution patterns and temporal area coverage changes (Hu et al., 2015, 2016).

6.3. Causes of the *Sargassum* bloom since 2011

Before satellites were used to map and quantify *Sargassum* blooms (Gower et al., 2006), assessment of *Sargassum* biomass was based on shipboard observations only (Butler, Morris, Cadwallader, & Stoner, 1983; Butler & Stoner, 1983; Huffard, von Thun, Sherman, Sealey, & Smith, 2014; Parr, 1939; Schell, Goodwin, & Siuda, 2015; Siuda, Schell, & Goodwin, 2016; Stoner, 1983). Most of these shipboard observations were focused on the Sargasso Sea, where no significant *Sargassum* biomass changes were found between 1933 and 1981 (Butler & Stoner, 1984). Recently, Schell et al. (2015) found *Sargassum* morphological changes in the Caribbean. Yet these shipboard surveys relied on neuston net tows that may have missed large *Sargassum* rafts as captured by synoptic and frequent satellite measurements. Then, what could cause the sudden increase in these MODIS-observed *Sargassum* coverages after 2011?

While it is extremely difficult to pinpoint the exact reason of a large-scale oceanic phenomenon, a preliminary effort was attempted to explain the observed long-term changes. We fully recognize that a thorough understanding requires multi-disciplinary efforts to analyze both physical and biological forcing, yet analysis of several environmental variables may provide some hints to address the following questions: Where do the *Sargassum* slicks originate? And, what caused the recent increases in the area coverage?

Indeed, although the MODIS statistics started in 2000, there is no record in either local newspaper or in fishermen's memory of any major *Sargassum* beaching event for the past 50–60 years prior to 2011 (Dr. Jean-Philippe Maréchal, Caribbean Global Coral Reef Monitoring Network (GCRMN) advisor, personal comm.), suggesting that there might be a significant change in the local environment in the past half century.

Daily image sequences were examined to determine the potential origin of the *Sargassum* slicks, similar to the methodology used in Hu and He (2008), to determine the origin of the *Ulva* bloom off Qingdao (China) in the Yellow Sea. Although several sequences did reveal the first appearance of *Sargassum* slicks and their temporal movements, it is hard to conclude that they originated from the location where they first observed. This may be due to the fact that many small *Sargassum* slicks are unlikely to be captured by coarse pixels resolution (Hu et al., 2015). It is more likely that *Sargassum* originates in a certain location, moves, and is detectable in MODIS AFAI imagery only when surface aggregation results in large, observable slicks (>2 m wide and >2 km long, see Section 6.2.2). Thus, this effort did not lead to any solid inference on the origin of *Sargassum* slicks. On the other hand, recent shipboard observations showed that *Sargassum* in the CWA region in 2015 had a different dominant form than in the Sargasso Sea, suggesting that the Sargasso Sea is unlikely to be the source region (Schell et al., 2015). This is supported by hindcast numerical models, which suggested that *Sargassum* may bloom in the north equatorial recirculation region (NERR) due to favorable environmental conditions (Johnson, Ko, Franks, Moreno, & Sanchez-rubio, 2013).

Excessive nutrient supply may be responsible for the increase in *Sargassum* biomass (Smetacek & Zingone, 2013). Could the temporal patterns be related to the Amazon River discharge and associated river plume? Fig. 12 shows that between May and August 2015 (the maximum *Sargassum* months in the maximum year), *Sargassum* slicks did appear in the vicinity of the Amazon plume (where the plume was inferred from elevated K_d490 values from the monthly mean K_d490 images. This is because K_d490 is highly correlated with colored dissolved organic matter rich in river plume, Hu,

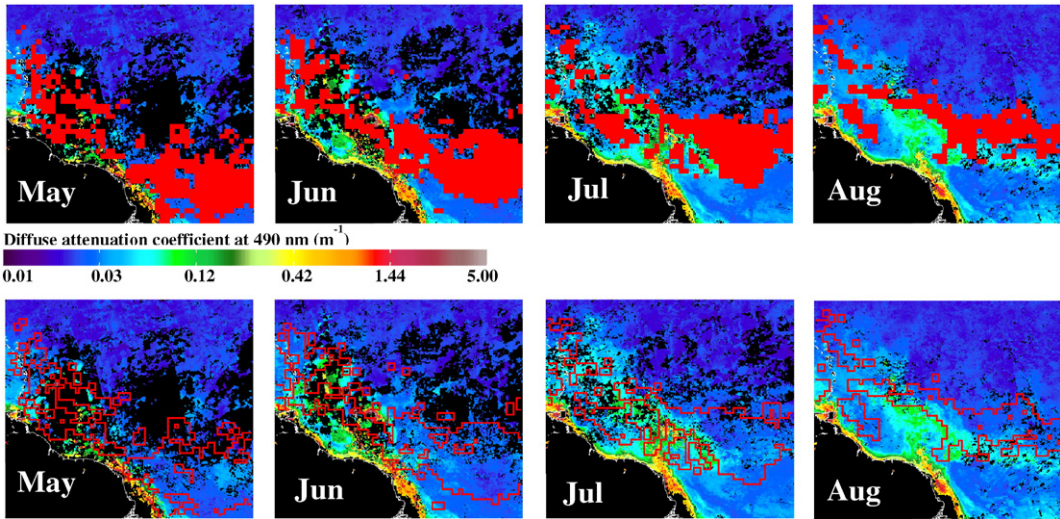


Fig. 12. MODIS monthly mean diffuse attenuation coefficient at 490 nm (K_d490, m^{-1}) from May to August 2015, overlaid with *Sargassum* coverage (red area in the top row and red outline in the bottom row). Here the *Sargassum* coverage is defined as fractional coverage $>0.05\%$.

Montgomery, Schmitt, & Muller-Karger, 2004). This, however, could simply be a coincidence as both the plume and the *Sargassum* slicks were driven by the same ocean currents. Indeed, the Amazon River

discharge (Fig. 13e) and the *Sargassum* area coverage does not appear to be correlative, suggesting that river discharge might not be the dominant reason for increased bloom activity.

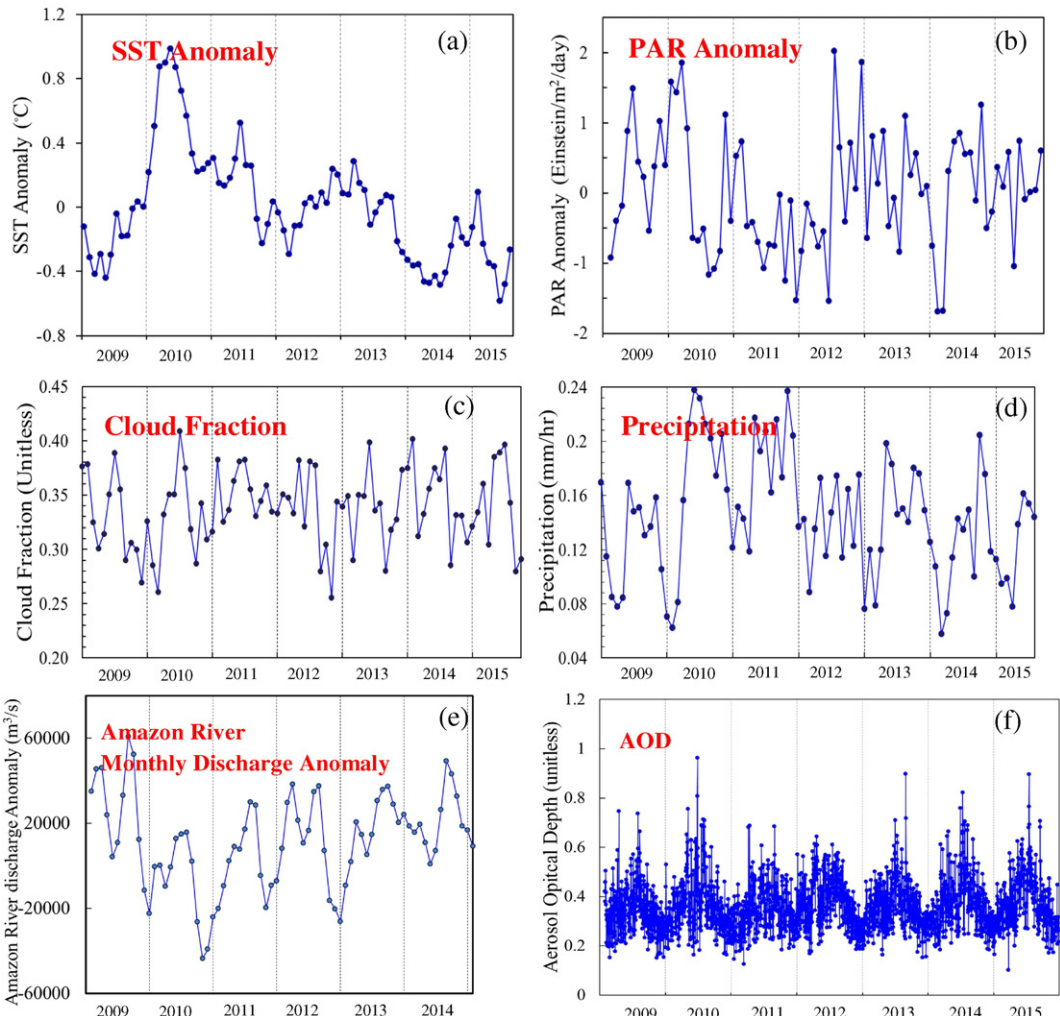


Fig. 13. Monthly mean values of several environmental variables over the CWA region. (a) Sea Surface Temperature (SST); (b) Photosynthetic Available Radiation (PAR); (c) cloud fraction; (d) precipitation rate; (e) Amazon River discharge anomaly; (e) aerosol optical depth (AOD).

Analysis of other environmental variables indicated that although PAR and cloud fraction did not show any apparent correlation with the *Sargassum* temporal patterns, a combination of SST, precipitation, and AOD might explain some of them. For example, precipitation was much higher in 2010 and 2011 than in other observable years. The higher than usual precipitation may have brought additional nutrients (iron) from aerosols (dust) to the surface ocean (Paerl et al., 1999), favoring *Sargassum* growth in the following years (2011 and 2012). The winter of 2014 showed lower SST (~0.4 °C lower than monthly mean climatology), possibly associated with stronger upwelling (or deeper mixing) than other years (Black et al., 1999; Peterson, Haug, Hughen, & Röhl, 2000; Weingartner & Weisberg, 1991) or with more African dust according to the correlation of North Atlantic SST with African dust proposed by Wang, Dong, Evan, Foltz, and Lee (2012) using a dataset back to 1950's (which may be excluded as no significant change in AOD is detected in Fig. 13f), providing more nutrients to *Sargassum* and resulting in blooms in 2014 and 2015. The same mechanism could also be used to explain the 2011 and 2012 blooms as SST in these two years was also lower than in other years. Therefore, the following hypothesis may be generalized from these visual interpretations: while the origin of the *Sargassum* is still unclear, the 2011 and 2012 blooms appear to be a result of the combined effect of higher precipitation (more atmospheric nutrients) and lower SST (deeper mixing or stronger upwelling), and the 2014 and 2015 blooms appear to be the result of deeper mixing or strong upwelling. AOD shows a strong seasonal pattern with more dust input in summer and less in winter (corresponds well with the annual cycle of African dust transport to the Caribbean Basin as mentioned in Prospero, Collard, Molinié, & Jeannot, 2014). This is positively correlated with the *Sargassum* temporal patterns in Fig. 9, suggesting dust input may stimulate *Sargassum* growth. Regardless, the exact mechanisms leading to the annual fluctuations and the 2015 anomaly in *Sargassum* coverage will still require a significant amount of multi-disciplinary effort to resolve. In the meantime, the distribution maps in Fig. 8, the long-term temporal patterns in Fig. 9, and those obtained from historical and recent shipboard observations (Butler & Stoner, 1983; Butler et al., 1983; Parr, 1939; Schell et al., 2015; Siuda et al., 2016; Stoner & Greening, 1984), may serve as guides on how to perform such a multi-disciplinary investigation.

6.4. Continuity and other considerations

The distribution patterns and long-term trends of *Sargassum* coverage, as revealed in Figs. 8 and 9, suggest that it is likely that *Sargassum* blooms may occur in future years. Given aging MODIS instruments (they were both designed for 5-year mission life but have been operational for >13 years), the question is whether the observations can be continued if one or both MODIS instruments cease to function? In other words, is one instrument enough? And, if both fail, what other instruments can be used?

To address these questions, statistics were generated from individual MODIS instruments and compared with those from combined observation platforms. Between 2009 and 2015, 9013 AFAI images were used to generate the statistics, of which 4953 were from MODISA and 4060 were from MODIST. Fig. 14 shows that when MODIST and MODISA were used separately, the estimated annual mean *Sargassum* coverage was nearly identical between 2009 and 2013, but showed slight differences (<20%) from the coverage estimates in 2014 and 2015 when both satellite platforms were combined. Thus, if and when one of instruments stops functioning in the future, reliable statistics can still be generated from the other one, with potentially <20% uncertainty as referenced against the combined observations.

The Visible Infrared Imaging Radiometer Suite (VIIRS) instrument has provided daily data since 2012. VIIRS has all required spectral bands to calculate a VIIRS AFAI. In addition, a VIIRS swath width (3000 km) is greater than a MODIS swath (2330 km), providing

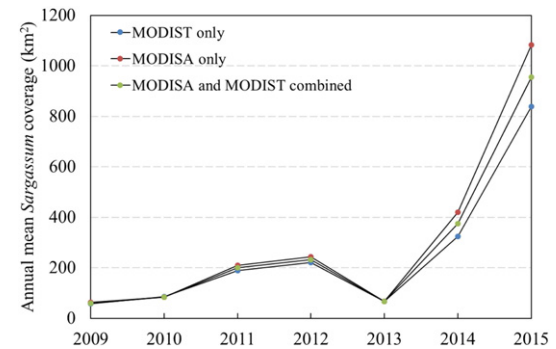


Fig. 14. Annual mean *Sargassum* coverage (km²) over the CWA region estimated from MODIST, MODISA, and MODIST/MODISA combined. The 2015 data contains data through 21 November 2015.

more data coverage than a single MODIS instrument. Therefore, even if both MODISA and MODIST stop functioning, VIIRS can be used to continue the *Sargassum* observations. Once proper cross-sensor calibration is achieved, VIIRS is expected to provide a seamless data record for the foreseeable future. The Ocean Land Colour Instrument (OLCI) onboard the Sentinel-3 satellite was launched on 16 February 2016. As a MERIS-heritage sensor (300-m resolution, 1400-km swath) but with more spectral bands (from 15 of MERIS to 21 of OLCI, Donlon et al., 2012), OLCI is also capable of providing AFAI and MCI products once data become available. We expect to perform the cross-sensor calibration on these sensors and generate VIIRS and OLCI AFAI data products soon.

The Pre-Aerosol, Cloud, and ocean Ecosystem (PACE) mission is currently planned at NASA (<http://pace.gsfc.nasa.gov>), with the aim of providing hyperspectral data at similar coverage and revisit frequency of MODIS. Such a hyperspectral mission is expected to not only provide continuity observations from MODIS and VIIRS but more importantly to provide diagnostic capacity to differentiate *Sargassum* from other floating materials (Dierssen et al., 2015; Hu et al., 2015). Likewise, NASA's Hyperspectral InfraRed Imager (HypIRI) mission (Lee et al., 2015) and Geostationary Coastal and Air Pollution Events (GEO-CAPE) mission (Fishman et al., 2012) will both have hyperspectral capacity for spectral diagnostics. In particular, the GEO-CAPE mission on a geostationary platform will enable multiple images a day at the same location, making it easier to avoid cloud cover and to track *Sargassum* movement using sequential images. This feature has been demonstrated already for tracking blooms of the green macroalgae *U. prolifera* in the Yellow Sea using the Geostationary Ocean Color Imager (GOCI) (Son, Min, & Ryu, 2012). Furthermore, the future Geostationary Operational Environmental Satellites – R Series (GOES-R) series will have two spectral bands in the red (640 nm) and NIR (860 nm), respectively, with a ground resolution of 1 km (Schmit et al., 2005). Once proven with sufficient SNRs, the GOES-R series may provide more frequent data than any other sensors to monitor and track *Sargassum* blooms.

The daily MODIS images have already served as useful guides to local residents of the Lesser Antilles Islands as well as other regions in the Intra-Americas Sea, and helped management agencies to prepare for *Sargassum* beaching events. Compared to the *Sargassum* Early Advisory System (SEAS) to forecast *Sargassum* beaching events using LANDSAT imagery (30-m resolution) and other ancillary data (Webster & Linton, 2013), the daily MODIS images have coarser spatial resolution but higher revisit frequency and more spatial coverage, thus enabling the derivation of long-term and large-scale perspectives on the size and trend of *Sargassum* blooms. Although it is difficult to pinpoint the reason of the recent blooms, one may still conclude that the blooms were not due to local pollution but to large-scale atmospheric and oceanic forcing, possibly related to weather fluctuations and climate change. The findings here may therefore provide unprecedented

information to help local residents to adapt and prepare for future *Sargassum* beaching events in a changing climate in order to sustain tourism and a healthy economy.

7. Conclusions

An objective method has been developed to quantify *Sargassum* distributions and area coverage from MODIS observations. The MODIS data were then used to generate distribution maps and area coverage between 2000 and 2015 over the Central West Atlantic region. While some of these results were reported previously using MERIS observations up to 2011 using a different method, this is the first time that a longer time series has been objectively developed which has revealed unprecedented *Sargassum* coverage patterns after 2011 ever since MODIS was put in orbit in 2000. In particular, *Sargassum* coverage in 2014 and 2015 was found to be significantly higher than in any previously observable year, with 2015 being the extremely anomalous year. Although it is currently difficult to pinpoint the reasons for these changes, the findings here may provide guidance on future multi-disciplinary studies to understand their origin, causes, and possible consequences to the ocean environment.

We want to emphasize that the data processing required to generate the statistics from low-level MODIS data is computationally expensive. Our initial effort was therefore dedicated to methodology development with the focus on the CWA region only. Our next step is to extend this methodology to the entire Intra-Americas Sea (including Caribbean Sea and Gulf of Mexico et al.), the Sargasso Sea, and the entire tropical Atlantic. Combined with ocean circulation and other data, a larger picture than presented here may provide more information to solve the puzzle of *Sargassum* origin, bloom transport, and future trends in a changing climate.

Notations

AFAI	Alternative Floating Algae Index
AIRS	Atmospheric Infrared Sounder
AOD	Aerosol optical depth
AUP	Area coverage using unweighted <i>Sargassum</i> Pixels
AWP	Area coverage using weighted <i>Sargassum</i> Pixels
CWA	Central West Atlantic (0 – 22°N, 63 – 38°W)
FAI	Floating Algae Index
GEO-CAPE	Geostationary Coastal and Air Pollution Events
GOCI	Geostationary Ocean Color Imager
GOES-R	Geostationary Operational Environmental Satellites – R Series
GOM	Gulf of Mexico
HICO	Hyperspectral Imager for the Coastal Ocean
HyspIRI	Hyperspectral InfraRed Imager
ITCZ	Inter Tropical Convergence Zone
LLR	Local Low Reflectance
LTR	Local Total Reflectance
MERIS	Medium Resolution Imaging Spectrometer (2002 – 2012)
MCI	Maximum Chlorophyll Index (MCI)
MODIS	Moderate Resolution Imaging Spectroradiometer (2000 – on Terra; 2002 – on Aqua)
MODISA	MODIS/Aqua
MODIST	MODIS/Terra
NASA	National Aeronautics and Space Administration
NDAI	Normalized Difference Algae Index
NDVI	Normalized Difference Vegetation Index
NERR	North Equatorial Recirculation Region
NIR	Near Infrared
NOAA	National Oceanic and Atmospheric Administration
OI	Optimum Interpolation
OLCI	Ocean and Land Color Instrument
OMI	Ozone monitoring instrument

PACE	Pre-Aerosol, Cloud, and ocean Ecosystem mission
PAR	Photosynthetically Available Radiation
Rrc	Rayleigh-Corrected Reflectance
SAI	Scale Algae Index
SeaDAS	SeaWiFS Data Analysis System
SEAS	<i>Sargassum</i> Early Advisory System
SeaWiFS	Sea-viewing Wide Field-of-view Sensor (1997–2010)
SEMs	Standard Error of the Means
SNR	Signal to noise ratio
SST	Sea Surface Temperature
SWIR	Short-Wave Infrared
T ₀	Global scope segmentation threshold
T _c	Threshold for cloud shadow detection using the LLR masking
T _s	Threshold for preliminary <i>Sargassum</i> -containing pixel extraction based on surface fitting
TOA	Top-of-atmosphere
TRMM	Tropical Rainfall Measuring Mission
VAS	Virtual Antenna System
VIIRS	Visible Infrared Imaging Radiometer Suite

Acknowledgment

This work was supported by the U.S. NASA Ocean Biology and Biogeochemistry program (NNX13AD08G, NNX14AL98G, NNX15AB13A). We thank the NASA OBPG for providing all MODIS data used in this study. Analyses and visualizations of the cloud fraction, AOD and precipitation used in this paper were produced with the Giovanni online data system, developed and maintained by the NASA GES DISC. We thank NOAA/OAR/ESRL PSD for providing the monthly mean SST data. Amazon River discharge data were acquired from the Brazilian National Water Agency with the assistance of Dr. Claudio Barbosa of Instituto Nacional de Pesquisas Espaciais (INPE) (Brazil). We thank Dr. Lian Feng (USF) for providing suggestions on cloud shadow masking, and Mr. Brock Murch for his various editorial comments. Two anonymous reviewers provided valuable comments and suggestions, whose effort is appreciated.

References

- Baith, K., Lindsay, R., Fu, G., & McClain, C. R. (2001). Data analysis system developed for ocean color satellite sensors. *Eos, Transactions American Geophysical Union*, 82(18), 202–205.
- Black, D. E., Peterson, L. C., Overpeck, J. T., Kaplan, A., Evans, M. N., & Kashgarian, M. (1999). Eight centuries of North Atlantic Ocean atmosphere variability. *Science*, 286(5445), 1709–1713.
- Butler, J. N., & Stoner, A. W. (1984). Pelagic *Sargassum*: Has its biomass changed in the last 50 years? *Deep Sea Research Part A. Oceanographic Research Papers*, 31(10), 1259–1264.
- Butler, J. N., Morris, B. F., Cadwallader, J., & Stoner, A. W. (1983). *Studies of Sargassum and the Sargassum community*. Bermuda Biological Station for Research, 22.
- Chinchor, N., & Sundheim, B. (1993). MUC-5 evaluation metrics. *Proceedings of the 5th Conference on Message Understanding* (pp. 69–78).
- Council, S. A. F. M. (Ed.). (2002). *Fishery management plan for pelagic Sargassum habitat of the South Atlantic region* (pp. 228). (<http://safmc.net/Library/pdf/SargFMP.pdf>).
- Dierssen, H. M., Chlus, A., & Russell, B. (2015). Hyperspectral discrimination of floating mats of seagrass wrack and the macroalgae *Sargassum* in coastal waters of Greater Florida Bay using airborne remote sensing. *Remote Sensing of Environment*, 167, 247–258. <http://dx.doi.org/10.1016/j.rse.2015.01.027>.
- Donlon, C., Berruti, B., Buongiorno, A., Ferreira, M. H., Féminas, P., Frerick, et al. (2012). The global monitoring for environment and security (GMES) sentinel-3 mission. *Remote Sensing of Environment*, 120, 37–57.
- Fishman, J., Iraci, L. T., Al-Saadi, J., Chance, K., Chavez, F., Chin, M., et al. (2012). The United States' next generation of atmospheric composition and coastal ecosystem measurements: NASA's Geostationary Coastal and Air Pollution Events (GEO-CAPE) mission. *Bulletin of the American Meteorological Society*, 93(10), 1547–1566. <http://dx.doi.org/10.1175/BAMS-D-11-00201.1>.
- Garcia, R. A., Fearn, P., Keesing, J. K., & Liu, D. (2013). Quantification of floating macroalgae blooms using the scaled algae index. *Journal of Geophysical Research: Oceans*, 118(1), 26–42.
- Gower, J., & King, S. (2011). Distribution of floating *Sargassum* in the Gulf of Mexico and the Atlantic Ocean mapped using MERIS. *International Journal of Remote Sensing*, 32, 1917–1929.

- Gower, J., Hu, C., Borstad, G., & King, S. (2006). Ocean color satellites show extensive lines of floating *Sargassum* in the Gulf of Mexico. *IEEE Transactions on Geoscience and Remote Sensing*, 44, 3619–3625.
- Gower, J., King, S., Borstad, G., & Brown, L. (2005). Detection of intense plankton blooms using the 709 nm band of the MERIS imaging spectrometer. *International Journal of Remote Sensing*, 26, 2005–2012.
- Gower, J., Young, E., & King, S. (2013). Satellite images suggest a new *Sargassum* source region in 2011. *Remote Sensing Letters*, 4, 764–773.
- He, M.-X., Liu, J., Yu, F., Li, D., & Hu, C. (2011). Monitoring green tides in Chinese marginal seas. *Handbook of satellite remote sensing image interpretation: Applications for marine living resources conservation and management* (pp. 111–124). Dartmouth, Canada: EU PRESPO and IOC/C.
- Hu, C. (2009). A novel ocean color index to detect floating algae in the global oceans. *Remote Sensing of Environment*, 113, 2118–2129.
- Hu, C., & He, M. X. (2008). Origin and offshore extent of floating algae in Olympic sailing area. *Eos, Transactions American Geophysical Union*, 89, 302–303.
- Hu, C., Barnes, B. B., Murch, B., & Carlson, P. (2014). Satellite-based virtual buoy system (VBS) to monitor coastal water quality. *Optical Engineering*, 53(5), 051402. <http://dx.doi.org/10.1117/1.OE.53.5.051402>.
- Hu, C., Cannizzaro, J., Carder, K. L., Muller-Karger, F. E., & Hardy, R. (2010b). Remote detection of *Trichodesmium* blooms in optically complex coastal waters: Examples with MODIS full-spectral data. *Remote Sensing of Environment*, 114, 2048–2058.
- Hu, C., Feng, L., Hardy, R. F., & Hochberg, E. J. (2015). Spectral and spatial requirements of remote measurements of pelagic *Sargassum* macroalgae. *Remote Sensing of Environment*, 167, 229–246. <http://dx.doi.org/10.1016/j.rse.2015.05.022>.
- Hu, C., Feng, L., Lee, Z., Davis, C. O., Mannino, A., McClain, C. R., & Franz, B. A. (2012). Dynamic range and sensitivity requirements of satellite ocean color sensors: Learning from the past. *Applied Optics*, 51, 6045–6062.
- Hu, C., Hardy, R., Ruder, E., et al. (2016). *Sargassum* coverage in the northeastern Gulf of Mexico during 2010 from Landsat and airborne observations: Implications for the Deepwater Horizon oil spill. *Marine Pollution Bulletin*, 107, 15–21. <http://dx.doi.org/10.1016/j.marpolbul.2016.04.045>.
- Hu, C., Li, D., Chen, C., Ge, J., Muller-Karger, F. E., Liu, J., et al. (2010a). On the recurrent *Ulva prolifera* blooms in the Yellow Sea and East China Sea. *Journal of Geophysical Research: Oceans*, 115, C05017. <http://dx.doi.org/10.1029/2009JC005561>.
- Hu, C., Montgomery, E. T., Schmitt, R. W., & Muller-Karger, F. E. (2004). The dispersal of the Amazon and Orinoco River water in the tropical Atlantic and Caribbean Sea: Observation from space and S-PALACE floats. *Deep sea research part II: Topical studies in oceanography*, 51, 1151–1171.
- Huffman, C. L., von Thun, S., Sherman, A. D., Sealey, K., & Smith, K. L., Jr. (2014). Pelagic *Sargassum* community change over a 40-year period: temporal and spatial variability. *Marine Biology*, 161(12), 2735–2751.
- Johnson, D. R., Ko, D. S., Franks, J. S., Moreno, P., & Sanchez-Rubio, G. (2013). The *Sargassum* invasion of the Eastern Caribbean and dynamics of the Equatorial North Atlantic. *Proceedings of the 65th Annual Gulf and Caribbean Fisheries Institute Conference* (pp. 102–103).
- Keesing, J. K., Liu, D., Fearn, P., & Garcia, R. (2011). Inter-and intra-annual patterns of *Ulva prolifera* green tides in the Yellow Sea during 2007–2009, their origin and relationship to the expansion of coastal seaweed aquaculture in China. *Marine Pollution Bulletin*, 62, 1169–1182.
- Lee, C. M., Cable, M. L., Hook, S. J., Green, R. O., Ustin, S. L., Mandl, D. J., & Middleton, E. M. (2015). An introduction to the NASA Hyperspectral InfraRed Imager (HypSIRI) mission and preparatory activities. *Remote Sensing of Environment*, 167, 6–19.
- Marmorino, G. O., Miller, W. D., Smith, G. B., & Bowles, J. H. (2011). Airborne imagery of a disintegrating *Sargassum* drift line. *Deep Sea Research Part I: Oceanographic Research Papers*, 58(3), 316–321.
- Maurer, A. S., De Neef, E., & Stapleton, S. (2015). *Sargassum* accumulation may spell trouble for nesting sea turtles. *Frontiers in Ecology and the Environment*, 13, 394–395.
- Oyesiku, O. O., & Egungyomi, A. (2015). Identification and chemical studies of pelagic masses of *Sargassum natans* (Linnaeus) Gaillón and *S. fluitans* (Borgesssen) Borgesens (brown algae), found offshore in Ondo State, Nigeria. *African Journal of Biotechnology*, 13(10), 1188–1193.
- Paerl, H. W., Willey, J. D., Go, M., Peierls, B. L., Pinckney, J. L., & Fogel, M. L. (1999). Rainfall stimulation of primary production in western Atlantic Ocean waters: Roles of different nitrogen sources and co-limiting nutrients. *Marine Ecology Progress Series*, 176, 205–214.
- Parr, A. E. (1939). Quantitative observations on the pelagic *Sargassum* vegetation of the western north Atlantic. *Bulletin of the Bingham Oceanographic Collection*, 6, 1–94.
- Patt, F. S., Barnes, R. A., Epée, R. E., Jr., Franz, B. A., Robinson, W. D., Feldman, G. C., et al. (2003). Algorithm updates for the fourth SeaWiFS data reprocessing. *NASA Tech. Memo.*, vol. 206892. Greenbelt, MD: National Aeronautics and Space Administration, Goddard Space Flight Center.
- Peterson, L. C., Haug, G. H., Hughen, K. A., & Röhl, U. (2000). Rapid changes in the hydrologic cycle of the tropical Atlantic during the last glacial. *Science*, 290, 1947–1951.
- Prospero, J. M., Collard, F. X., Molinié, J., & Jeannot, A. (2014). Characterizing the annual cycle of African dust transport to the Caribbean Basin and South America and its impact on the environment and air quality. *Global Biogeochemical Cycles*, 28, 757–773.
- Robinson, W. D., Franz, B. A., Patt, F. S., Bailey, S. W., & Werdell, P. J. (2003). Masks and flags updates. *SeaWiFS Postlaunch Technical Report Series*. NASA Tech. Memo. 2003–206892, 2003.
- Rooker, J. R., Turner, J. P., & Holt, S. A. (2006). Trophic ecology of *Sargassum*-associated fishes in the Gulf of Mexico determined from stable isotopes and fatty acids. *Marine Ecology Progress Series*, 313, 249–259.
- Schell, J. M., Goodwin, D. S., & Siuda, A. N. (2015). Recent *Sargassum* inundation events in the Caribbean. *Oceanography*, 28(3), 8–10. <http://dx.doi.org/10.5670/oceanog.2015.70>.
- Schmit, T. J., Gunshor, M. M., Menzel, W. P., Gurka, J. J., Li, J., & Bachmeier, A. S. (2005). Introducing the next-generation Advanced Baseline Imager on GOES-R. *Bulletin of the American Meteorological Society*, 86(8), 1079–1096.
- Shi, W., & Wang, M. (2009). Green macroalgae blooms in the Yellow Sea during the spring and summer of 2008. *Journal of Geophysical Research: Oceans*, 114, C12010. <http://dx.doi.org/10.1029/2009JC005513>.
- Siuda, A., Schell, J., & Goodwin, D. (2016). Unprecedented proliferation of novel pelagic *Sargassum* form has implications for ecosystem function and regional diversity in the Caribbean. *Ocean Sciences Meeting*, 22–26 February 2016, New Orleans, LA, USA.
- Smetacek, V., & Zingone, A. (2013). Green and golden seaweed tides on the rise. *Nature*, 504(7478), 84–88.
- Son, Y. B., Min, J. -E., & Ryu, J. -H. (2012). Detecting massive green algae (*Ulva prolifera*) blooms in the Yellow Sea and East China Sea using geostationary ocean color imager (GOCI) data. *Ocean Science Journal*, 47(3), 359–375.
- Stoner, A. W. (1983). Pelagic *Sargassum*: Evidence for a major decrease in biomass. *Deep Sea Research Part A: Oceanographic Research Papers*, 30(4), 469–474.
- Stoner, A. W., & Greening, H. S. (1984). Geographic variation in the macrofaunal associates of pelagic *Sargassum* and some biogeographic implications. *Marine Ecology Progress Series*, 20, 185–192. <http://dx.doi.org/10.3354/meps020185>.
- Subramaniam, A., Brown, C. W., Hood, R. R., Carpenter, E. J., & Capone, D. G. (2002). Detecting *Trichodesmium* blooms in SeaWiFS imagery. *Deep-Sea Research Part II*, 49, 107–121.
- Székely, M. D., Guedes, P. M., Baeta-Neves, M. H., & Oliveira, E. N. (2012). Verification of *Sargassum natans* (Linnaeus) Gaillón (Heterokontophyta: Phaeophyceae) from the Sargasso Sea off the coast of Brazil, western Atlantic Ocean. *Checklist*, 8, 638–641.
- Szekielda, K. H., Marmorino, G. O., Bowles, J. H., & Gillis, D. (2010). High spatial resolution spectrometry of rafting macroalgae (*Sargassum*). *Journal of Applied Remote Sensing*, 4(1), 043529. <http://dx.doi.org/10.1117/1.3431044> (April 28, 2010).
- Wang, C., Dong, S., Evan, A. T., Foltz, G. R., & Lee, S. K. (2012). Multidecadal covariability of North Atlantic sea surface temperature, African dust, Sahel rainfall, and Atlantic hurricanes. *Journal of Climate*, 25, 5404–5415. <http://dx.doi.org/10.1175/JCLI-D-11-0413.1>.
- Webster, R. K., & Linton, T. (2013). Development and implementation of *Sargassum* Early Advisory System (SEAS). *Shore & Beach*, 81(3), 1–6.
- Weingartner, T. J., & Weisberg, R. H. (1991). On the annual cycle of equatorial upwelling in the central Atlantic Ocean. *Journal of Physical Oceanography*, 21, 68–82.
- Witherington, B., Hirama, S., & Hardy, R. (2012). Young sea turtles of the pelagic *Sargassum*-dominated drift community: Habitat use, population density, and threats. *Marine Ecology Progress Series*, 463, 1–22.
- Woodcock, A. H. (1993). Winds subsurface pelagic *Sargassum* and Langmuir circulations. *Journal of Experimental Marine Biology and Ecology*, 170, 117–125.
- Wylie, D., Jackson, D. L., Menzel, W. P., & Bates, J. J. (2005). Trends in global cloud cover in two decades of HIRS observations. *Journal of Climate*, 18, 3021–3031.